Geomorphic response to the Lateglacial–Holocene transition in high Alpine regions (Sanetsch Pass, Swiss Alps)

ELENA SERRA, PIERRE G. VALLA, NATACHA GRIBENSKI, FABIO GUEDES MAGRANI, JULIEN CARCAILLET, REYNALD DELALOYE, BERNARD GROBÉTY AND LUC BRAILLARD

Serra, E., Valla, P. G., Gribenski, N., Guedes Magrani, F., Carcaillet, J., Delaloye, R., Grobéty, B. & Braillard, L.: Geomorphic response to the Lateglacial–Holocene transition in high Alpine regions (Sanetsch Pass, Swiss Alps). *Boreas*. https://doi.org/10.1111/bor.12480. ISSN 0300-9483.

Several palaeoclimatic archives have documented the pronounced climatic and environmental change associated with the Lateglacial–Holocene transition in the European Alps. However, the geomorphic response to this major environmental transition has only been punctually investigated. In this study, we propose a detailed reconstruction of post-Last Glacial Maximum palaeoenvironmental conditions and geomorphic connectivity in the Sanetsch Pass area (2252 m a.s.l., western Swiss Alps) based on a multi-method approach combining geomorphological and sedimentological field investigations with quantitative sedimentology and geochronology. Samples for sediment characterization (grain size, micromorphology and X-ray diffraction) and geochronology (optically stimulated luminescence and ^{10}Be surface exposure dating) were collected from three representative landforms of the study area: a high-elevation silty deposit covered by patterned ground, an alluvial fan, and a hummocky moraine covered by rockfall deposits. Our results reveal the geomorphic history of the three deposits and their connectivity through sediment cascade. These results highlight the development of rapid and most probably transient landscape changes in high Alpine regions during the Lateglacial–Holocene transition, with an increase in sediment flux and the establishment of paraglacial and periglacial geomorphic processes.

Elena Serra (elena.serra@geo.unibe.ch), Natacha Gribenski and Fabio Guedes Magrani, Institute of Geological Sciences, University of Bern, Baltzerstrasse 1+3, CH-3012 Bern, Switzerland and Oeschger Centre for Climate Change Research, University of Bern, Hochschulstrasse 4, CH-3012 Bern, Switzerland; Pierre G. Valla, University of Grenoble Alpes, University of Savoie Mont Blanc, CNRS, IRD, IFSTTAR, ISTerre, 38000 Grenoble, France and Institute of Geological Sciences, University of Bern, Baltzerstrasse 1+3, CH-3012 Bern, Switzerland and Oeschger Centre for Climate Change Research, University of Bern, Hochschulstrasse 4, CH-3012 Bern, Switzerland; Julien Carcaillet, University of Grenoble Alpes, University of Savoie Mont Blanc, CNRS, IRD, IFSTTAR, ISTerre, 38000 Grenoble, France; Reynald Delaloye, Bernard Grobéty and Luc Braillard, Department of Geosciences, University of Fribourg, Ch. du Musée 4+6, CH-1700 Fribourg, Switzerland;

High-elevation Alpine regions are active environments, where landforms are constantly re-shaped by the interplay between a variety of geomorphic processes. Throughout the Quaternary, the nature and dominance of these processes have been largely determined by climatic oscillations between glacial and interglacial conditions. During glacial periods, glacier erosion, sediment transport and deposition leave behind characteristic landforms and deposits such as U-shaped valleys, glacial cirques, polished bedrock, moraines and erratic boulders (e.g. Benn & Evans 2014). During or soon after glacier retreat at the glacial/interglacial transition, glacial processes are gradually replaced by paraglacial and periglacial processes, which transiently transform the ice-free landscape (Church & Ryder 1972; Ballantyne 2002; French 2007; Mercier & Etienne 2008). Paraglacial processes involve various geomorphic agents (hillslope, fluvial, aeolian) resulting in a wide range of depositional and erosional landforms (e.g. rockfall deposits, debris cones, alluvial fans, gully incisions and aeolian drapes; Ballantyne 2002; Cossart *et al.* 2008; Borgatti & Soldati 2010; Cossart *et al.* 2013; Geilhausen *et al.* 2013; Gild *et al.* 2018). Periglacial processes are also present and give origin to permafrost-related landforms like rock glaciers and patterned ground (French 2007; Colombo *et al.* 2016).

The European Alps were repeatedly glaciated during the Late Pleistocene, with glacier expansion culminating at the Last Glacial Maximum (LGM, 26.5–19.0 ka ago; Clark *et al.* 2009; Wirsig *et al.* 2016a). Post-LGM warming and rapid ice decay were followed by episodes of glacier stillstands and re-advances during the Lateglacial period (Lateglacial stadials, 19.0–11.6 ka ago; Ivy-Ochs *et al.* 2007; Hippe *et al.* 2014; Ivy-Ochs 2015), due to temporary climate deteriorations (Schmidt *et al.* 2012). Following the Younger Dryas (YD, 12.7–11.6 ka ago; Ivy-Ochs *et al.* 2007) and the Early Holocene Preboreal Oscillation cold event (11.4–11.3 ka ago; Rasmussen *et al.* 2007; Schimmelpfennig *et al.* 2012), Alpine glaciers eventually retreated and remained behind the ice limit of the Little Ice Age (LIA, 1300–1860 CE; Hanspeter *et al.* 2005; Ivy-Ochs *et al.* 2009; Steinemann *et al.* 2020), in response to Early and Middle Holocene abrupt warming (Schimmelpfennig *et al.* 2012).

Palaeoenvironmental conditions during the Lateglacial and at the Holocene transition have been investigated through several palaeoclimate proxies (Heiri *et al.* 2014). However, the geomorphic response to this major environmental transition has been only punctually examined, focusing on specific geomorphic processes like rockfall activity (e.g. Zerathe *et al.* 2014; Ivy-Ochs *et al.* 2017) or fluvial incision (e.g. Korup & Schlunegger 2007; Valla *et al.* 2010; Rolland *et al.* 2017). Likewise, the timing of paraglacial activity, as well as the question of sediment cascade and landscape connectivity, are still poorly understood (Mercier & Etienne 2008 and references therein).

Our study aimed to contribute to the reconstruction of post-LGM palaeoenvironmental conditions and geomorphic connectivity within high-altitude Alpine regions. We focused on the Sanetsch Pass area (2252 m a.s.l., western Swiss Alps; Fig. 1) where multiple geomorphic processes have left an extensive record of landforms and sediment deposits during the Lateglacial and the Holocene (Fig. 2). Three landforms representative of the high Alpine landscape were investigated: a silty deposit covered by patterned ground, an alluvial fan and a hummocky moraine covered by rockfall deposits (Figs 1, 2, 3). These three deposits were selected with the goals of (i) reconstructing their geomorphological history, (ii) investigating a potential connectivity between the different records and (iii) assessing the suitability of glacial, paraglacial and periglacial landforms as proxies for palaeoenvironmental reconstruction in high Alpine regions. To that aim, we performed a detailed geomorphological and sedimentological field investigation and collected samples for multi-methodological analyses on the different landforms.

Study area and sampling locations

The study area is located next to the Sanetsch Pass (2252 m a.s.l., western Swiss Alps; Fig. 1). The local bedrock is composed of Cretaceous and Palaeogene sedimentary rocks belonging to the Helvetic Diablerets and Wildhorn nappes (Badoux *et al.* 1959; Masson *et al.* 1980). Three geological units are of particular interest for our study: calcareous shales containing ~20% of fine detrital quartz (Palfris Formation; Föllmi *et al.* 2007) form the Arpille Ridge, siliceous limestones (Helvetic Kieselkalk Formation; Föllmi *et al.* 2007) form the Arpelistock cliff, and quartzose sandstones (Fruttli Member of the Klimsenhorn Formation, Menkveld-Gfeller 1997) form a ~5-m-thick layer at the top of the calcareous Les Montons cliff (Fig. 2).

The Sanetsch Pass is currently ice-free, with the nearest glacier front (Tsanfleuron Glacier) ~3 km to the south-west (Fig. 1). During the LGM, the Rhône glacier reached an altitude of about 2000 m a.s.l. in the main valley above Sion (Fig. 1; Bini *et al.* 2009). The Sanetsch Pass area was partly covered by ice with an estimated average thickness of ~200 m and some mountain peaks were protruding above the ice surface as nunataks (Bini *et al.* 2009). The Tsanfleuron glacier was flowing both northwards and southwards from the pass, as testified by lateral morainic ridges (Fig. 2; Badoux *et al.* 1959). Following the deglaciation of the Swiss foreland *c.* 21 ka ago (Ivy-Ochs *et al.* 2004), the Rhône Valley became ice-free *c.* 17 ka ago (Hantke 1992; Hinderer 2001). The onset of sedimentation in the Pond Emines (at 2288 m a.s.l., ~1 km south-west from the Sanetsch Pass; Fig. 2) at *c.* 12 ka ago (Berthel *et al.* 2012), and the apparent post-12 ka exposure ages (Steinemann *et al.* 2020) of glacially polished bedrock outside the Tsanfleuron LIA moraine (~1 km west of the Sanetsch Pass; Fig. 2) imply ice-free conditions at the Sanetsch Pass during or soon after the YD. Paraglacial and periglacial processes following the deglaciation have resulted in a rich record of landforms reflecting the transient landscape evolution (Fig. 2). Three representative landforms of the Sanetsch Pass landscape are investigated in the present study (Figs 2, 3).

The first landform consists of a thin sediment blanket draping a bedrock platform located on the southern slope of the Arpelistock peak, in contact with glacial deposits from a small local glacier (ARP site, 2660–2715 m a.s.l., ~0.23 km^2 in area; Fig. 3A). The surface of the ARP deposit exhibits locally a polygonal patterned ground (Fig. 3B; Gobat & Guenat 2019). The second landform is an alluvial fan located in the plain north of the Sanetsch Pass (CRE site, 2090–2130 m a.s.l., 0.14 km^2 in area; Fig. 3A, C). The third landform is a hummocky moraine located north of the plain (SAN site, 2040–2100 m a.s.l., 0.13 km^2 in area; Fig. 3A, C, D). The distinct hummocky morphology, with hills up to a few metres high, is partially covered by rockfall deposits composed of sandstone and limestone boulders detached from the nearby overhanging cliff (Les Montons peak; Figs 2, 3D).

Material and methods

Geomorphological and sedimentological field investigation

In the present study, we performed a new geomorphological mapping over an area of ~16 km^2 around the Sanetsch pass (Fig. 2), based on the sheet St-Léonard (1286) (Badoux *et al.* 1959) of the Geological Atlas of Switzerland (1:25 000). To this aim, we combined the geomorphological map of Quaternary superficial deposits (Badoux *et al.* 1959) with new field investigations and remote sensing mapping based on the swissALTI3D DEM and orthophotos (swisstopo).

Detailed stratigraphical outcrops were logged for the ARP and CRE deposits. Two stratigraphical profiles (~40 cm deep) were dug out in the ARP high-elevation silty deposit, below the polygonal patterned ground

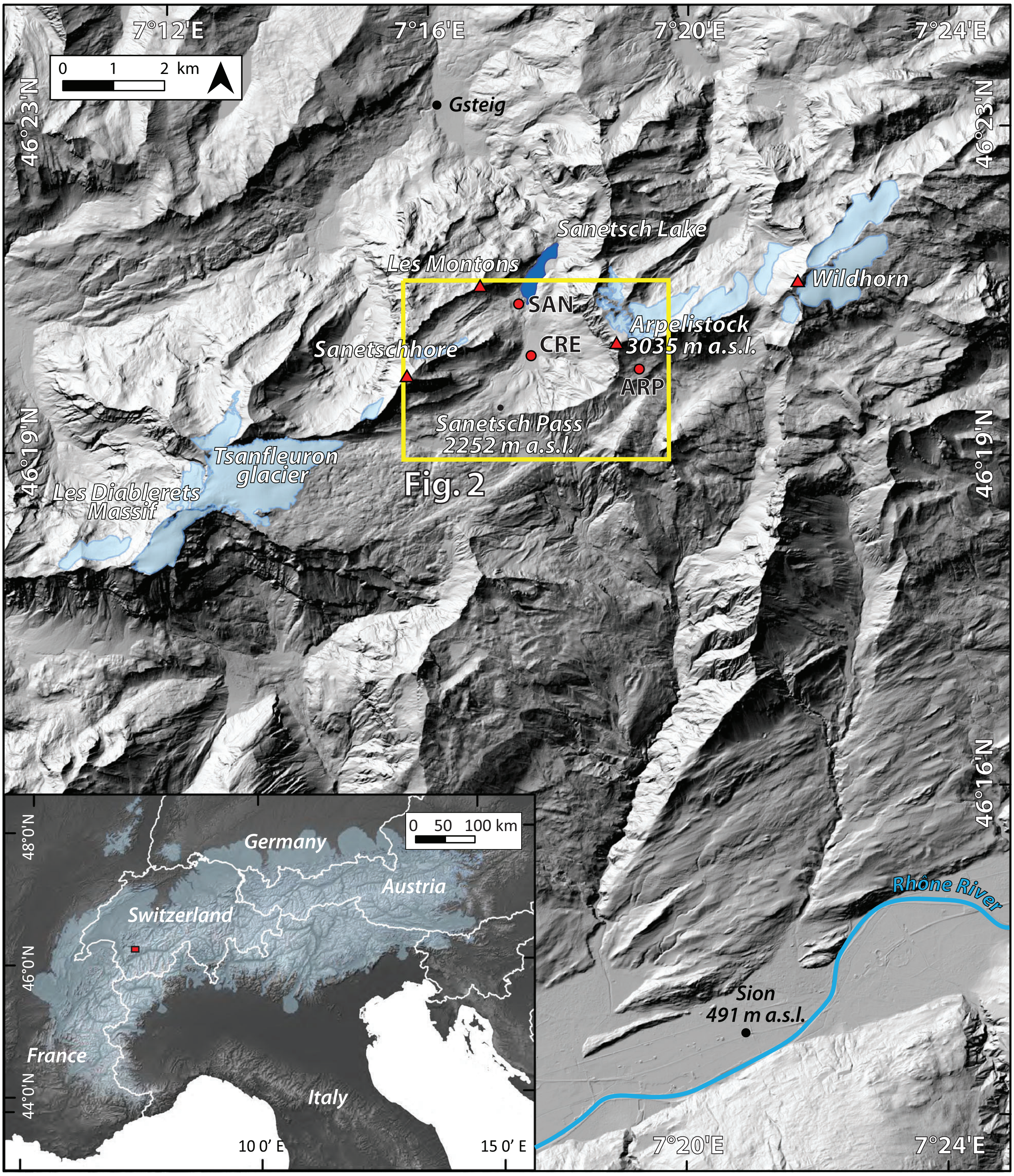

Fig. 1. Location of the study area (swissALTI3D DEM from swisstopo, authorization 5701367467/000010). Present-day glaciers, main peaks around the Sanetsch Pass and the Rhône River are marked. The yellow box indicates the extent of the geomorphological map presented in Fig. 2. Inset shows location of the Sanetsch Pass (red box) within Switzerland and the European Alps, with the LGM ice extent (Ehlers & Gibbard 2004).

(Fig. 3B). The CRE log was recorded from a natural outcrop exposed in a gully incising the alluvial fan (4.5 m deep; Fig. 3C). Sedimentary units were identified based on their grain-size range, sorting, clast shape, compaction, sedimentary structures, colour and lithology. Reaction to HCl in the field and the

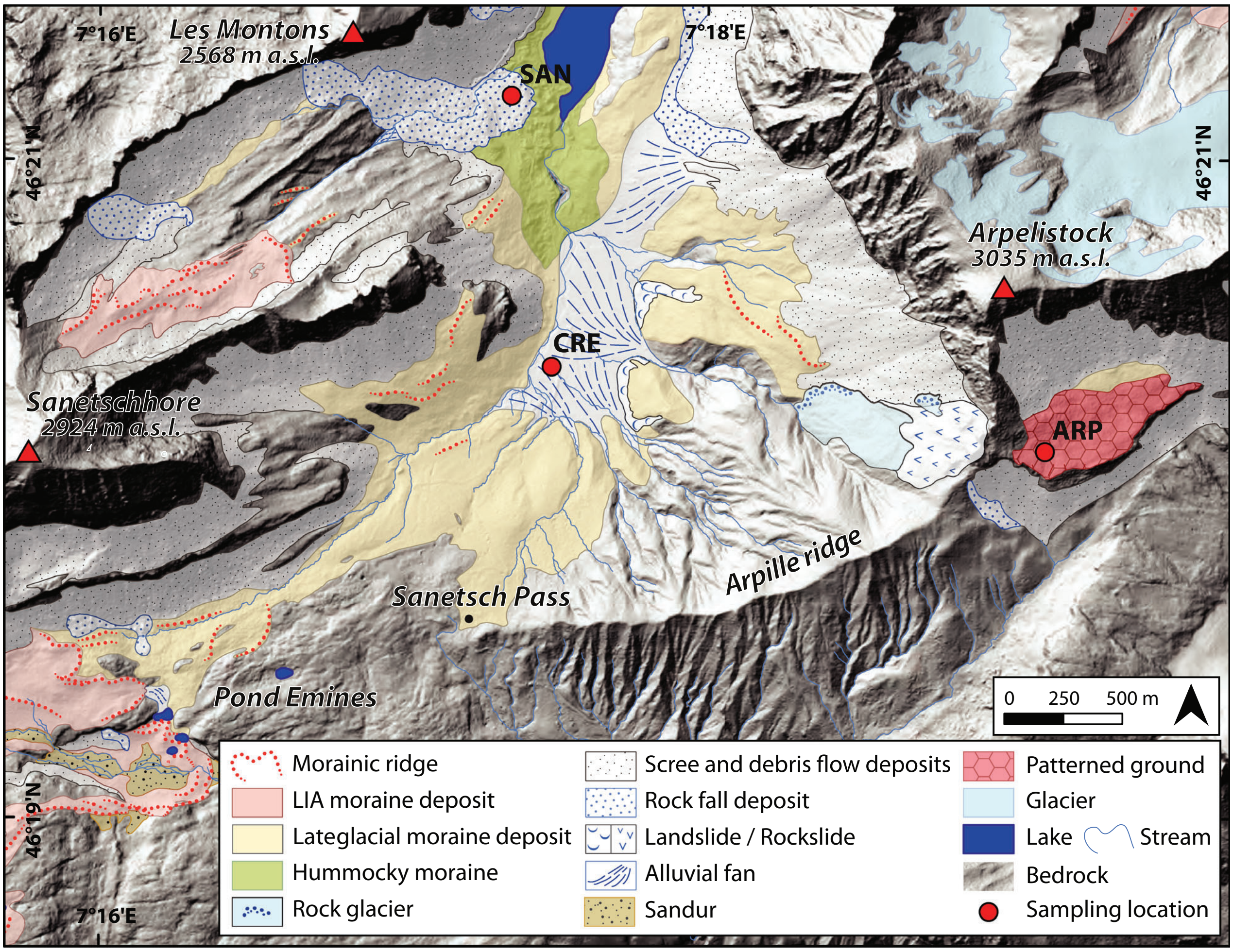

Fig. 2. Detailed map of the Quaternary deposits occurring in the study area (swissALTI3D DEM from swisstopo, authorization 5701367467/000010). The different Quaternary deposits and the three study sites are shown: high-elevation platform covered by patterned ground (ARP), alluvial fan (CRE) and hummocky moraine and rockfall deposits (SAN). The hillshade area corresponds to bedrock (mainly limestones, as well as shales for the Arpille ridge, see text for details).

nature of contacts between individual units were also recorded.

Grain size, micromorphology and optical petrography

Eight bulk sediment samples were collected for grain-size analyses (G1–G6 from CRE site, G7 and G8 from ARP site; Figs 5 and 4, respectively), in order to understand the genesis of the ARP and CRE deposits and the potential connectivity between them. Conventional grain-size distribution measurements were carried out by sieving the air-dried sand and granule/pebble fractions (Rivière 1977; Hadjouis 1987). Analyses of the silt and clay fractions were performed using a laser Malvern MS20 diffraction system (Department of Environmental Sciences, University of Basel, Switzerland). Sorting indexes (So) were calculated using millimetre units ($So = (D_{75}/D_{25})^{0.5}$, where D_{25} and D_{75} are respectively the first and the third quartile of the grain-size distribution), providing different sediment sorting categories: very well sorted ($So < 2.5$), well sorted (So between 2.5 and 3.5), normally sorted (So between 3.5 and 4.5) and poorly sorted ($So > 2.5$).

Three CRE undisturbed sediment samples were collected in Kubiena boxes (8×11 cm) for micromorphological analyses (M1–M3; Fig. 5), with the aim to identify depositional and postdepositional features in the alluvial fan sediments. The samples were first air-dried, impregnated with an acetone-diluted epoxy resin and then cut with a diamond saw (Department of Environmental Sciences, University of Basel, Switzerland). Two covered thin sections (4.5×4.5 cm) per sample were prepared (Th. Beckmann, Braunschweig, Germany) and examined optically on a Leitz DM-RXP microscope, both in plane-polarized and crossed-polarized light. Bedrock thin sections were additionally prepared (Department of Geosciences, University of

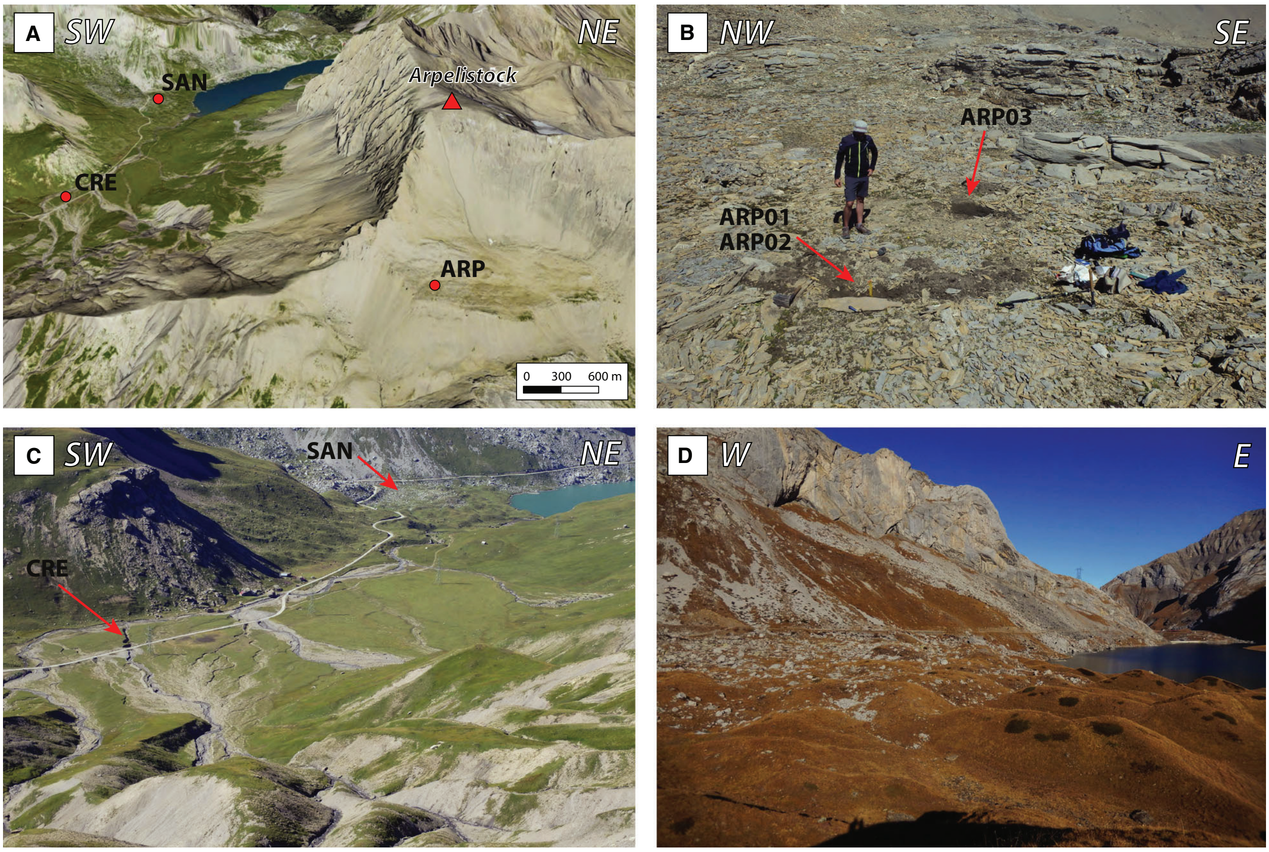

Fig. 3. Field photographs. A. General view of the three study sites (see Fig. 2 for locations) looking from the south (orthophoto and swissALTI3D DEM from swisstopo, authorization 5701367467/000010). B. High-elevation platform covered by sorted polygonal patterned ground (ARP site), on the southern slope of the Arpelistock peak. Arrows indicate the locations of the two stratigraphical sections and the ARP samples. C. View from the Arpille ridge on the Sanetsch valley, with arrows indicating the location of the alluvial fan log (CRE site) and the hummocky moraine with overlying rockfall deposits (SAN site), in contact with the Sanetsch artificial lake. D. Hummocky moraine (SAN site) partially covered by rockfall boulders derived from Les Montons cliff.

Fribourg, Switzerland) and analysed for four bedrock samples representative of the catchment lithology (two from the siliceous limestone, L1 and L2, and two from the calcareous shale, S1 and S2; Table S1), in order to obtain further information on the silicate fraction of the bedrock (grain shape and size) and to discuss the potential connectivity between the local bedrock and the CRE sediments.

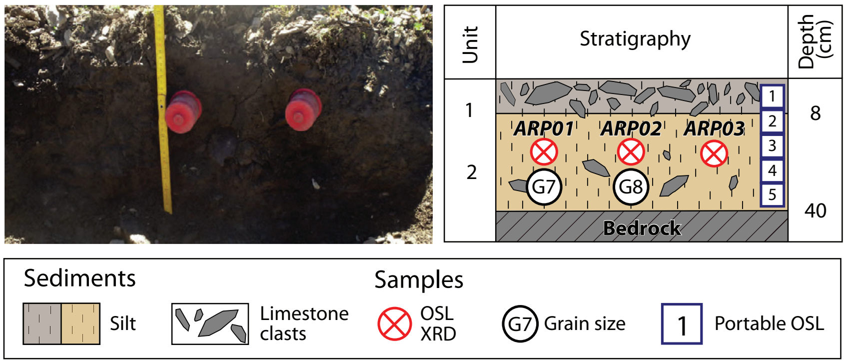

Fig. 4. Stratigraphy of the ARP site (left: photograph, right: log). Sedimentological units and samples collected for the different analyses are represented: XRD (ARP01 and ARP03, red crossed circles), grain size (G7 and G8, black circles), conventional OSL (ARP01–ARP03, red crossed circles) and portable OSL (arp01–arp05, blue boxes). Unit colours refer to the stratigraphical description in Table S3. The deposit lies on top of non-weathered siliceous limestone bedrock.

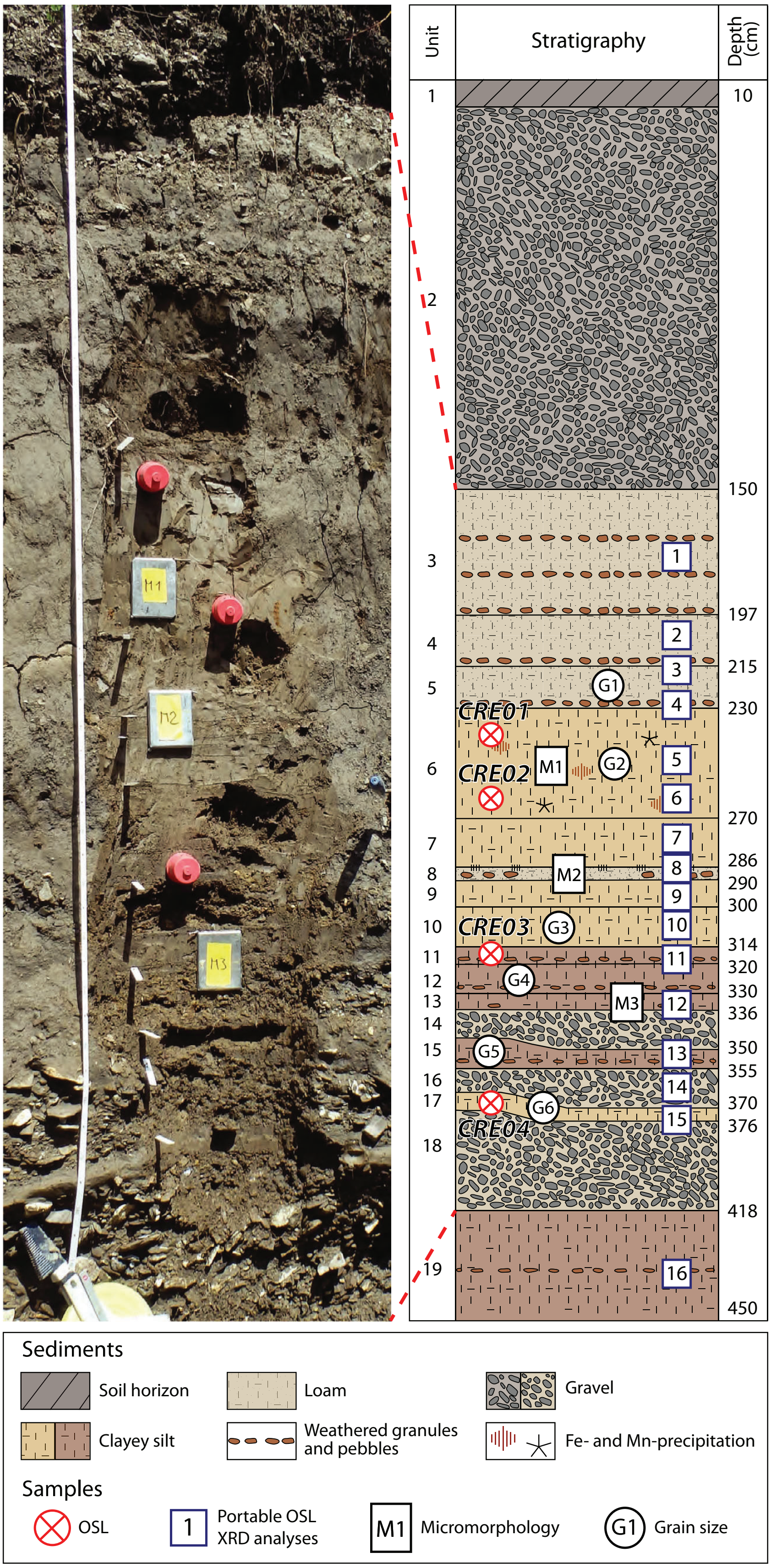
M1
M2
M3
Unit
Stratigraphy
Depth (cm)
1
2
3
4
5
6
7
8
9
10
11
12
13
14
15
16
17
18
19
10
150
197
215
230
270
286
290
300
314
320
330
336
350
355
370
376
418
450
CRE01
CRE02
CRE03
CRE04
G1
G2
G3
G4
G5
G6
M1
M2
M3
1
2
3
4
5
6
7
8
9
10
11
12
13
14
15
16
Sediments
Soil horizon
Loam
Gravel
Clayey silt
Weathered granules and pebbles
Fe- and Mn-precipitation
Samples
OSL
1
Portable OSL XRD analyses
M1
Micromorphology
G1
Grain size

Fig. 5. Stratigraphy of the CRE site (left: photograph, right: log). Sedimentological units and samples collected for the different analyses are shown: XRD (CRE01–CRE16, blue boxes), grain size (G1–G6, black circles), micromorphology (M1–M3, black rectangles), conventional OSL (CRE01–CRE04, red crossed circles) and portable OSL (cre01–cre16, blue boxes). Red dashed lines show the extent of the photograph in proportion to the log. Unit colours refer to the stratigraphical description in Table S4.

X-ray diffraction and geochemistry

X-ray diffraction (XRD) analyses were performed on a total of 22 samples, including 18 bulk sediment samples from CRE and ARP sites (CRE01–CRE16, Fig. 5; ARP01 and ARP03, Fig. 4) and four bedrock samples (L1, L2, S1, S2), to gain information on their mineral composition and assess sediment provenance and potential connectivity of the ARP and CRE deposits. Bulk sediments and bedrock samples were ground with a mechanical crusher, and sample powders were analysed through a Rigaku Ultima IV diffractometer system using Cu-Kα radiation (Department of Geosciences, University of Fribourg, Switzerland). Mineral identification was performed using the Rigaku's PDXL-2 software and the ICDD Powder Diffraction File 2017 database (International Centre for Diffraction Data). Mineral quantification was made by Rietveld refinement (Rietveld 1969), with weighted residuals of the whole pattern (Rwp) and the goodness of fit (GOF) considered as Rietveld fit criteria (Toby 2006). In the present refinements, Rwp and GOF values range from 4.84 to 6.74% and from 1.73 to 2.90, respectively.

Concentrations of total carbon (TC) and total inorganic carbon (TIC) were measured on the same ARP and CRE sediment samples, using a Bruker G4 Icarus elemental analyser (Institute of Geology, University of Bern, Switzerland). The percentage of total organic carbon (TOC) was determined from the difference between TC and TIC. These analyses and calculations were performed to examine the potential presence of palaeosols in the deposits.

Geochronology

Portable optically stimulated luminescence – Luminescence signal intensities were measured for the CRE (cre01–cre16; Fig. 5) and ARP (arp01–arp05; Fig. 4) sites, with the aim of investigating potential stratigraphical variations in the luminescence response, possibly reflecting differences in sediment provenance and depositional environment. Indeed, the luminescence signal of bulk sediment is mainly dependent, amongst other factors, on the pre-deposition light exposure of sediments (i.e. signal resetting or 'bleaching'; King *et al.* 2014) and on the post-deposition signal accumulation during burial time due to surrounding irradiation (i.e. sediment age; Sanderson & Murphy 2010). A few grams of sample was collected at different depths along the ARP and CRE stratigraphy, and sealed from light exposure. We quantified total photon counts on two replicates of each bulk sediment sample (without chemical pre-treatment) using the SUERC portable OSL reader (Sanderson & Murphy 2010), following the measurement sequence of Muñoz-Salinas *et al.* (2014). The measurement sequence (150 s in total) comprises a first cycle of infrared-stimulated luminescence, targeting feldspar minerals within the bulk sediment (IRSL, 30 s), and a second cycle of blue-stimulated luminescence targeting quartz (hereafter referred to as optically stimulated luminescence, OSL, 60 s), separated by 10 s of dark counts. Two additional periods (10 s) of dark counts bracketed each measurement sequence. Final (IRSL and OSL) photon counts were obtained by averaging between the two replicate measurements of each sediment sample.

Conventional optically stimulated luminescence dating – Seven fine-grain samples were collected for conventional luminescence dating from the CRE alluvial fan (CRE01–CRE04; Fig. 5) and the ARP high-elevation platform (ARP01–ARP03; Fig. 4), to constrain sediment deposition chronology. By combining conventional and portable luminescence measurements, we determined the true depositional chronology of the deposits, taking into account potential pre-depositional partial bleaching or post-depositional sediment reworking (i.e. resulting in age overestimation or underestimation, respectively).

Samples were collected with opaque plastic tubes pounded into fresh sediment surface (Nelson *et al.* 2015). Under subdued laboratory illumination, samples were treated with HCl (32%) and H_2O_2 (30%) to remove carbonates and organic components, respectively. Sedimentation in Atterberg cylinders (based on Stokes' Law) was used to extract the 4–11 μm grain-size fraction. Half of the extracted 4–11 μm fraction was additionally treated with H_2SiF_6 (30%) to obtain pure quartz (only ARP03 did not provide enough material for quartz purification). Polymineral and quartz separates were settled on 10-mm diameter stainless steel discs for subsequent luminescence analyses.

All conventional luminescence measurements were carried out using TL/OSL DA-20 Risø readers, equipped with a calibrated $^{90}Sr/^{90}Y$ beta source (Institute of Geology, University of Bern, Switzerland). Luminescence signals were detected using an EMI 9235QA photomultiplier tube, in the UV region through a 7.5 mm Hoya U-340 transmission filter and in the blue region through a Schott BG-39 and L.O.T.-Oriel D410/30 nm filter combination, for quartz OSL and polymineral IRSL measurements, respectively.

OSL and/or IRSL measurements were performed according to sample mineral composition. OSL equivalent dose (D_e) measurements were conducted on quartz separates of two ARP samples (ARP01 and ARP02) and on all the CRE samples. A post-IR OSL protocol was applied (Table S2A), which includes an IRSL stimulation at 50 °C (100 s) prior to the blue OSL stimulation (at 125 °C for 100 s; Lowick *et al.* 2015). IRSL D_e measurements were conducted on polymineral (non-separated) fractions for all the ARP samples using the post-IR IRSL protocol of Buylaert *et al.* (2009) (this protocol targets feldspar luminescence signal only; Table S2B). After a preheat treatment (250 °C for 60 s), luminescence measurement cycles of this modified single-aliquot regenerative-dose (SAR) protocol (Murray & Wintle 2000) consist of a first IRSL stimulation at 50 °C (100 s) followed by a second IRSL stimulation at 225 °C (100 s). A 40-s IRSL stimulation at 290 °C was added at the end of each SAR cycle in order to limit signal carry-over throughout successive cycles (Wallinga *et al.* 2007). No post-IR IRSL measurements were performed on CRE samples due to the absence of feldspar IRSL signal. Fading rates (*g*-value; Aitken 1985) were measured on aliquots used for D_e determination, following Auclair *et al.* (2003). Final fading corrected D_e values were calculated following the fading correction procedure of Huntley & Lamothe (2011), using the Luminescence R package (Kreutzer *et al.* 2012). Signals used for data analysis were integrated over the first 1.2–2.4 s minus the following 2.6–8 s for quartz OSL measurements, and over the first 1.2–10 s minus the last 90–99 s for polymineral IRSL measurements. Dose–response curves were constructed using an exponential fitting. Recycling ratios within 15% of unity and recuperation within 10% of the natural dose were used as acceptance criteria for the single-aliquot data. The suitability of the two applied protocols was confirmed by preheat-plateau (for quartz OSL), and residual and dose-recovery tests (Wintle & Murray 2006). For all the samples, residual doses <2% of the natural D_e and recovered doses within 10% of unity were measured.

About 200 g of bulk sediment material was collected from the surrounding of each sample to determine the environmental dose rate. The material was desiccated at 60 °C to enable water content quantification. U, Th and K activities were measured using high-resolution gamma spectrometry (Department of Chemistry and Biochemistry, University of Bern, Switzerland; Preusser & Kasper 2001) and were employed, together with the measured water content, as inputs for final dose rate determination through the Dose Rate and Age Calculator (DRAC; Durcan *et al.* 2015). Final ages were calculated using the central age model (CAM; Galbraith & Roberts 2012).

^{10}Be surface exposure dating – Three rockfall-derived sandstone boulders lying on the hummocky moraine, one on a flat area, one on a hummock ridge and one in an intra-hummock hollow (boulders ~2 m wide and 1 m high, SAN site; Fig. 3C), were sampled for ^{10}Be surface exposure dating, in order to obtain a minimum age constraint for the hummocky moraine formation. Samples were collected with hammer and chisel from flat surfaces on top of the boulders, with evidence of minimal erosion (Gosse & Phillips 2001). Sample crushing and sieving were performed to isolate the 250–400 μm grain-size fraction. Quartz was isolated using magnetic separation and repeated leaching in a H_2SiF_6-HCl mixture. Conventional chemical treatment adapted from Brown *et al.* (1991) and Merchel & Herpers (1999) was followed to complete ^{10}Be extraction (GTC platform, ISTerre, University Grenoble Alpes, France). ^{10}Be/^{9}Be ratios were measured at ASTER French National AMS facility (CEREGE, Aix-en-Provence, France; Arnold *et al.* 2010) against the in-house Be standard (Braucher *et al.* 2015), whose assumed isotope ratio is 1.191×10^{11}. Correction for a full process blank ratio of ^{10}Be/^{9}Be = $5.4\pm0.6\times10^{-15}$ was applied.

Surface exposure ages were computed with the online CREp program (Martin *et al.* 2017; https://crep.otelo.univ-lorraine.fr/#/init). Calculations were performed using a ^{10}Be production rate by neutron spallation at sea level and high latitude (SLHL) of 4.16 ± 0.10 at g^{-1} a^{-1} (Claude *et al.* 2014) scaled at the sample sites using the LSDn scaling scheme (Lifton *et al.* 2014). The ERA-40 reanalysis data set (Uppala *et al.* 2005) and the Lifton-VDM2016 geomagnetic database (Lifton 2016) were used to correct atmospheric pressure and geomagnetic field fluctuations, respectively. Corrections for topographic shielding based on field measurements were also applied (Dunne *et al.* 1999). For assessing the effect of potential post-depositional surface covering (e.g. snow) or surface degradation processes, two end-member scenarios were considered: one without any post-depositional correction and one including snow cover and surface-erosion corrections. For surface-erosion correction, an erosion rate of 1 mm ka^{-1} was applied, following the argument of Wirsig *et al.* (2016b). The snow cover correction factor was computed for all boulders following eq. (3.76) in Gosse & Phillips (2001), considering 6 months per year persistence of a 50-cm-thick snow cover (Wirsig *et al.* 2016b), a snow density of 0.3 g cm^{-3} and a spallation attenuation length in snow of 109 g cm^{-2} (Delunel *et al.* 2014).

Results

Geomorphological and sedimentological field investigation

We present an updated map of superficial deposits in Fig. 2, showing the Quaternary deposits occurring in the study area and the location of the three study sites (ARP, CRE and SAN).

Sedimentological observations for ARP and CRE deposits are summarized in the stratigraphical logs shown in Figs 4 and 5, respectively (detailed descriptions are given in Tables S3 and S4). The stratigraphy of the ARP deposit (Fig. 4, Table S3) consists of two sediment units lying on top of non-weathered siliceous limestone bedrock. The 10-cm-thick top unit (unit 1) is clast-supported, with siliceous limestone fragments in a silty matrix. The 30-cm-thick basal unit (unit 2) consists of a silty layer with a well-developed platy structure, containing few siliceous limestone fragments.

The stratigraphy of the CRE alluvial fan (Fig. 5, Table S4) displays the current soil horizon (unit 1) and the recent (i.e. Holocene) coarse alluvial fan deposit (unit 2) in the first 1.5 m of depth. Underneath, a succession of three categories of sediment units can be observed: homogenous clayey silt (units 6, 7, 9, 10, 17, called 'fine layers' hereafter), silty clay or loam containing weathered granules and pebbles (units 3, 4, 5, 8, 11, 12, 13, 15, 19, called 'heterogeneous layers' hereafter), and gravel layers clast-supported with imbricated elements (units 14, 16, 18).

Grain size and micromorphology

Grain-size distributions (Fig. 6) show strong similarities between the ARP silty unit (unit 2, samples G7 and G8), and the CRE fine (units 6, 10, 17, samples G2, G3 and G6) and heterogeneous (units 5, 12, 15, samples G1, G4 and G5) layers. Frequency curves are multi-modal and characterized by one primary peak around 35 µm (coarse silt), a secondary peak around 4–8 µm (fine/very fine silt), and a minor peak around 150 µm (fine sand). An additional minor peak around 10^4 µm (pebble) is also visible for samples G4 (CRE site, heterogeneous layer) and G8 (ARP site), which reflects the presence of some isolated clasts as observed in the stratigraphy (Figs 4, 5). Median grain-size values (D_{50}) range between 11 and 16 µm (fine silt). Calculated So vary between 2.7 and 3.4, reflecting good sorting (with the exception of G4 and G8, which have a So of 5.5 and 4.5, respectively, but reduced to 3.3 and 2.9 if only the clayey, silty and sandy fractions are considered).

Fig. 7 highlights the main micromorphological features observed in thin sections from the CRE alluvial fan. Thin section M1 (fine unit 6; Fig. 7A) displays a moderately developed subangular blocky microstructure in the clayey silt, expressed by slickensides associated with mottling. A low proportion (<2%) of small lithic fragments (<2 mm; not visible in Fig. 7A but similar to the one shown in Fig. 7C) containing quartz grains (20 to 300 µm size) is also recognized. In thin sections M2 (fine unit 7; Fig. 7B) and M3 (heterogeneous unit 13), well-developed horizontal laminae (1 to 5 mm thick) with normal grading are observed. In addition, the lower part of thin section M2 (heterogeneous unit 8; not visible in Fig. 7B) contains a higher proportion (5–10%) of weathered (partly decarbonated) lithic fragments (2–5 mm) in a clayey-silty matrix. Thin section M3 (heterogeneous units 12 and 13; only unit 13 shown in Fig. 7C) shows ~40% of weathered (partly to completely decarbonated) lithic fragments (3–10 mm) containing quartz grains (20 to 150 µm size), which are embedded in a clayey-silty carbonated matrix. These fragments present different weathering stages, but no weathering cortex on their edges. Lastly, bedrock thin sections display quartz grains of 10 to 150 µm size (the main population ranging between 30 and 50 µm), representing 5–15% of the

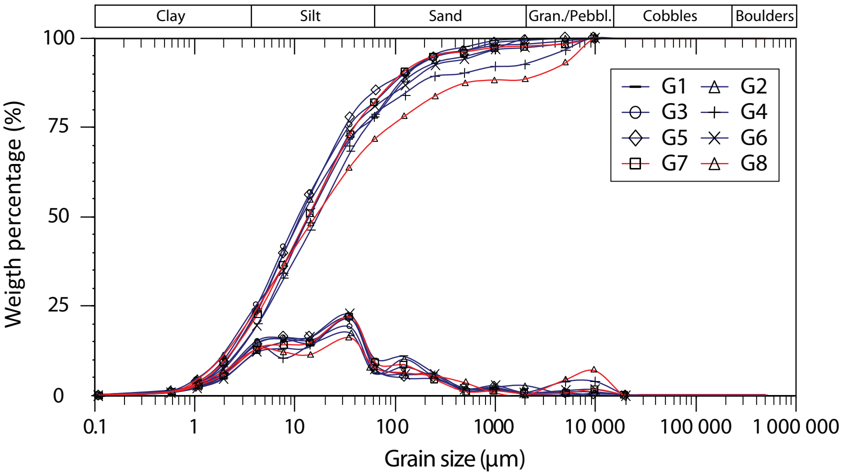

Fig. 6. Grain-size distributions of ARP (G7 and G8, in red) and CRE (G1–G6, in blue) samples. Individual cumulative (top) and frequency (bottom) curves show strong similarities between ARP and CRE sites. The distribution curves of G4 (CRE) and G8 (ARP) are slightly different because of the presence of small clasts within the samples (see individual peak at ~10^4 µm). Grain-size distribution data are reported in Table S6.

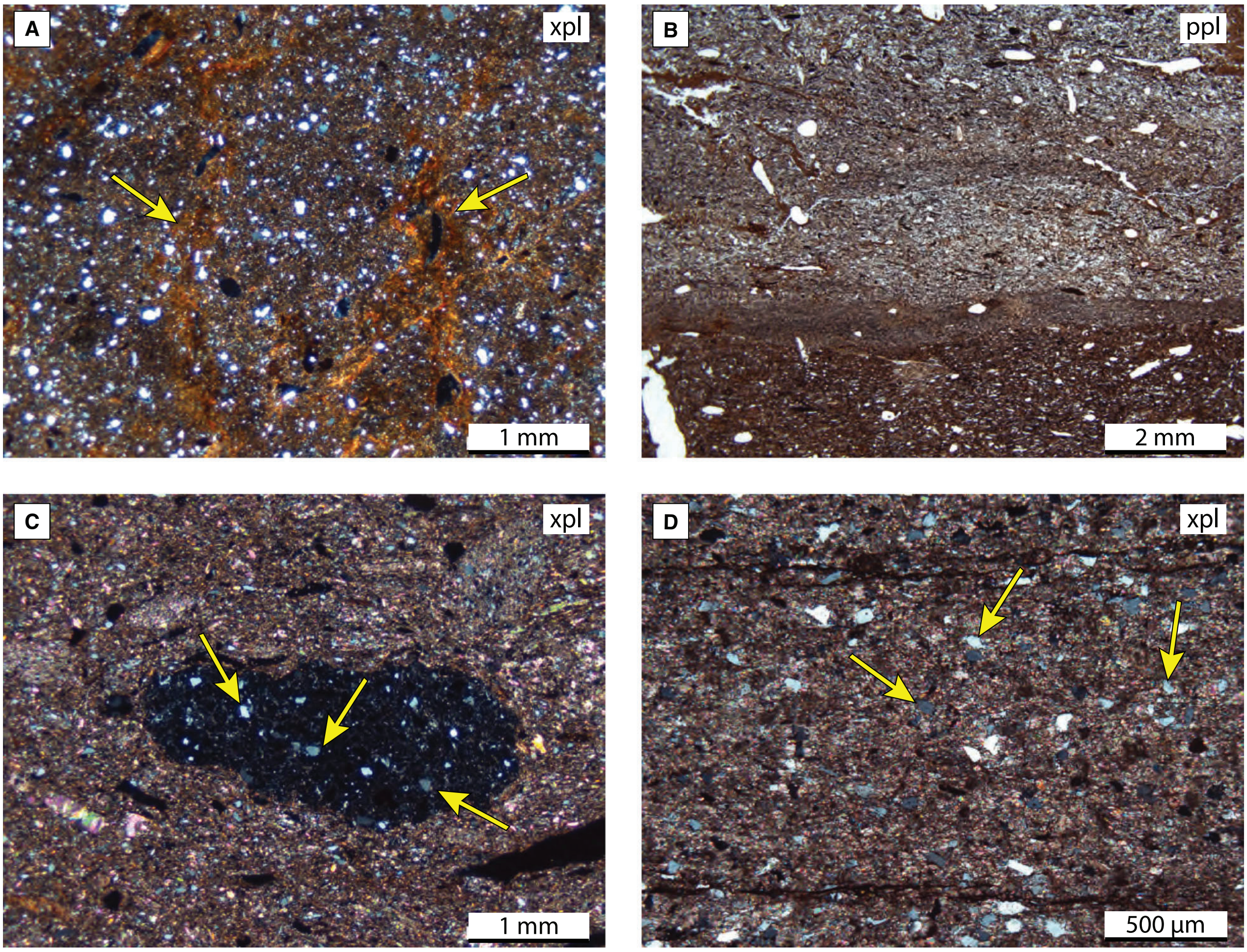

Fig. 7. Main micromorphological features observed in CRE fine and heterogeneous units (A–C) and bedrock thin section (D). A. Thin section M1 (unit 6) shows a blocky microstructure developed in the silty sediments expressed by slickensides associated with mottling (reddish zones indicated by yellow arrows). B. Detail of thin section M2 showing the well-developed horizontal parallel lamination present within unit 7. C. Detail of thin section M3 with weathered, decarbonated lithic fragments containing quartz grains (greyish grains, examples highlighted by yellow arrows), in a clayey-silty carbonated matrix (unit 13). D. Bedrock thin section (calcareous shales S1) showing abundant quartz grains (greyish grains, examples highlighted by yellow arrows). xpl = crossed-polarized light; ppl = plane-polarized light.

siliceous limestone and 15–30% of the calcareous shales (Fig. 7D).

X-ray diffraction and geochemistry

XRD results show four distinct average mineralogical compositions (Fig. 8). Bedrock samples (samples L1–L2 and S1–S2) present similar composition, largely dominated by carbonates (55–66% calcite and up to 5% dolomite). Silicates are secondary components, mainly represented by quartz (23–33%) and micas (3–16%), with some chlorite appearing only in the calcareous shales (S1–S2, up to 4%). ARP sediment samples (ARP01 and ARP03) are carbonate-free and contain 67–70% of quartz and 19% of micas as main components (with up to 8% of chlorite and 4–7% of albite). For CRE samples, two main groups can be distinguished from the mineralogical compositions. Nine samples (CRE02, 03, and 05 to 11) are carbonate-free and contain mainly quartz (40–54%), micas (36–52%) and chlorite (1–14%). The seven other samples (CRE01, 04, and 12 to 16) are characterized by variable calcite content (5–39%), in addition to quartz (32–43%), micas (23–43%) and chlorite (6–11%) components. CRE04 also contains a small percentage of albite (11%), as found in the ARP samples. Geochemistry analyses result in low TOC percentages for all the CRE (0.3–1.2%) and ARP (0.8 and 1.2%) samples.

Geochronology

Portable OSL measurements – ARP and CRE depth profiles for luminescence signal intensity are shown in Fig. 9 (samples arp01–arp05) and Fig. 10 (samples cre01–cre16), respectively (luminescence counts are reported in Table S5). For the ARP site (Fig. 9), both the quartz OSL and feldspar IRSL intensity profiles

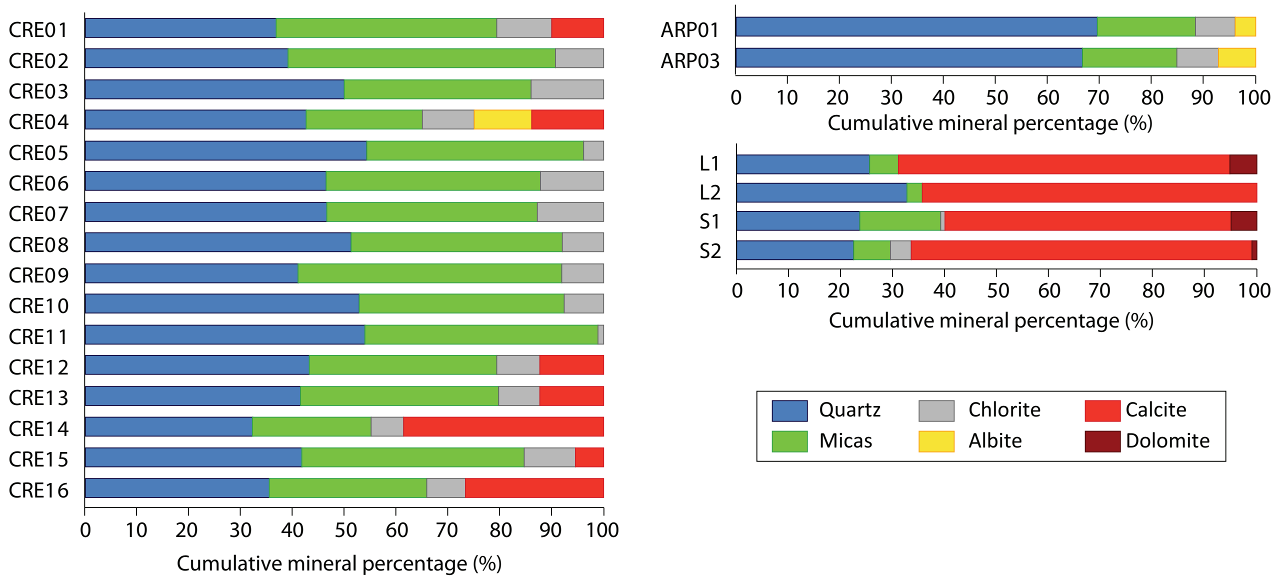

Fig. 8. XRD bulk mineralogical compositions of CRE (CRE01–CRE16), ARP (ARP01 and ARP03) and bedrock (L1–L2: siliceous limestone, S1–S2: calcareous shale) samples. Cumulative mineral percentages are reported in Table S7.

could be measured, with more than one order of magnitude difference between OSL (10^3–10^4 counts) and IRSL (10^1–10^2 counts) signals. While the IRSL counts increase consistently with depth (Fig. 9B), the OSL intensity profile is more complex: sample arp03 displays large uncertainty due to the significant difference between the two replicate measurements, and sample arp05 deviates significantly from the increasing signal trend with depth (Fig. 9A).

For the CRE site, the general low-feldspar content in the analysed sediments, as highlighted by XRD analyses (Fig. 8), prevented the measurement of IRSL signal along the section, and only an OSL profile could be obtained (Fig. 10). The measured profile does not show a stratigraphical coherence (i.e. luminescence signal intensity increasing with depth), but alternates between two signal intensity groups characterized by low (20–25×10^3 counts) and high (30–50×10^3 counts) OSL counts. These two groups correspond respectively to fine (low signal intensities) and heterogeneous (high signal intensities) layers (Fig. 10).

Conventional OSL dating – Sample specific information and results, including D_e values, relevant dose rate data and final CAM ages (Galbraith & Roberts 2012), are shown in Tables 1 and 2, and Figs 9 and 10. Both OSL and IRSL ages were obtained for two ARP samples (ARP01 and ARP02; Fig. 9), while only an IRSL age was measured for sample ARP03 (due to the lack of material for quartz purification). ARP final IRSL and OSL ages range between 2.5 and 7 ka, with high variability between samples and signals despite sample collection at relatively similar depths within unit 2 (~25 cm deep; Fig. 4). For both ARP01 and ARP02, the IRSL and OSL ages appear to differ without any systematic trend (i.e. younger IRSL age for ARP01, the opposite for ARP02).

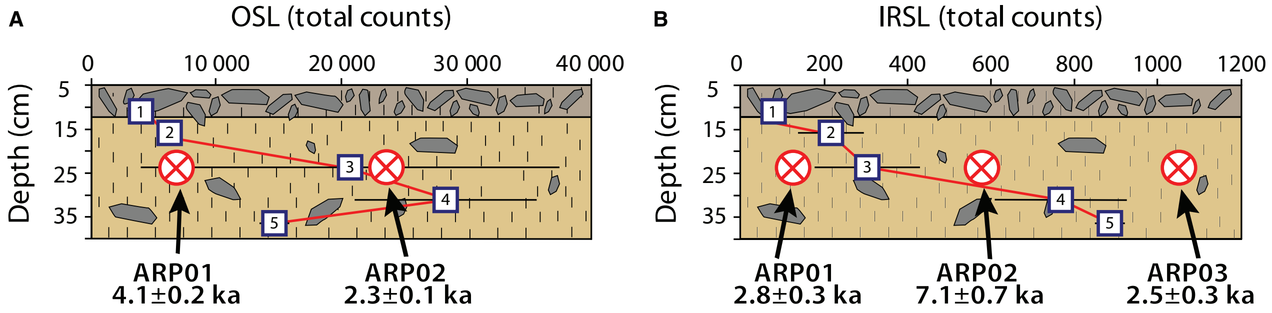

Fig. 9. Portable and conventional luminescence measurements for the ARP site. A. OSL signal intensity profile and quartz OSL ages. B. IRSL signal intensity profile and polymineral IRSL ages. See Fig. 4 for the legend of the stratigraphical column.

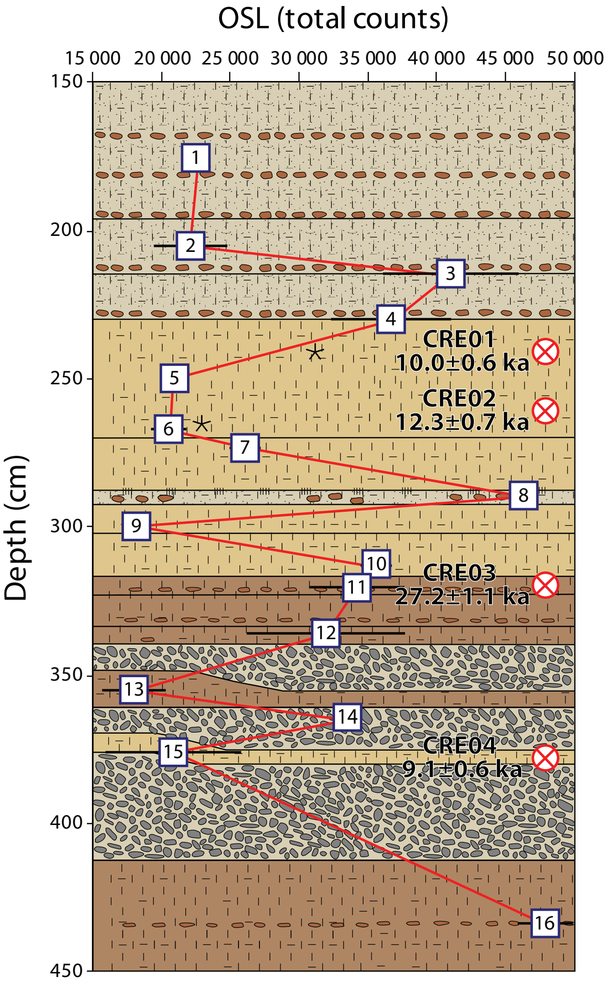

Fig. 10. Portable and conventional luminescence measurements for the CRE site. OSL signal intensity profile and quartz OSL ages are shown. See Fig. 5 for the legend of the stratigraphical column.

Quartz OSL data for the CRE site (Fig. 10) result in two age populations. The first age population concentrates around 11 ka (weighted-average age of 10.5±1.6 ka) and corresponds to samples CRE01 (10.0±0.6 ka), CRE02 (12.3±0.7 ka) and CRE04 (9.1±0.6 ka). All three samples were collected from fine layers (unit 6 for samples CRE01 and CRE02, unit 17 for sample CRE04). A significantly older age of 27.2±1.1 ka was obtained from sample CRE03, coming from a heterogeneous layer containing pebbles (unit 11). No post-IR IRSL measurements were performed on CRE samples due to the absence of feldspar IRSL signal.

^{10}Be surface exposure dating – Sample specific information, as well as measured ^{10}Be concentrations and calculated exposure ages (with and without erosion and snow corrections), are summarized in Table 3 and Fig. 11. A high consistency of the ^{10}Be exposure ages obtained for the three SAN sandstone boulders is evident (9.3±0.4, 9.4±0.4 and 9.8±0.4 ka, without snow and erosion corrections). The three boulder ages agree within uncertainty and yield a weighted-average age estimates of 9.5±0.3 ka (no snow and erosion corrections) and 10.3±0.3 ka (with snow and erosion corrections).

Discussion

Landform and sediment (post-)depositional histories

High-elevation platform (ARP) – Field stratigraphical observations (Table S3) and the different results obtained from the multi-method approach suggest (i) that the silty sediments (unit 2) from the ARP high-elevation platform correspond to an aeolian deposit covered by *in situ* produced cryoclasts (i.e. bedrock limestone clasts derived from freeze and thaw cycles), and (ii) that the whole deposit has been reworked by recent (possibly still ongoing) cryoturbation.

Excluding the coarser grain-size fraction (>2 mm, most probably deriving from isolated cryoclasts) from G7 and G8 grain-size analyses (Fig. 6), the good sorting indexes (2.5 and 3.3, respectively) and the dominance of the silty fraction (D_{50} = 10.1 and 11.1 μm, respectively) point towards loess deposit (*sensu stricto*; Pye 1987; Smalley 1995; Muhs 2013). The multi-modal grain-size distributions further suggest a local deflation source, with three main modes (4–8, 35 and 150 μm; Fig. 6) roughly corresponding to silicate fractions (micas and quartz) from local bedrock (10–150 μm; Fig. 7D). Observed Lateglacial aeolian deposits at low elevations in the Rhône Valley (Sion and Bex; Fig. 1) show unimodal grain-size distributions (main mode between 20 and 150 μm), very good sorting (1.8) and D_{50} of 35–45 μm (Guélat 2013; and pers. comm. 2016). We interpret the different grain-size characteristics between ARP and Rhône Valley loess as the result of a mixed provenance with both local and allochthonous input for the ARP deposit.

Several arguments allow us to exclude the hypothesis that the ARP silty sediments derive from *in situ* weathering of the underlying siliceous limestone (L1–L2; Fig. 8): (i) the sharp (with no weathering) contact between the base of the ARP aeolian deposit and the underlying bedrock, (ii) the complete absence of carbonates, and (iii) the presence of albite in ARP samples (ARP01 and ARP03; Fig. 8). The albite content (4–7%) supports the hypothesis of an allochthonous component within the ARP aeolian deposit, possibly related to the Rhône Valley loess at lower elevations, which is dominated by quartz, micas, chlorite and feldspar mineralogy (Spaltenstein 1984; Guélat pers. comm. 2016). Such a loessic input was indeed highlighted in a nearby soil profile located 1.7 km south of the Sanetsch Pass (Spaltenstein 1985). However, XRD analyses alone cannot discriminate the dominant source area(s) between Alpine or more distal origin (e.g. Martignier

Table 1. Sample luminescence details and corresponding quartz OSL dating results. For analytical details about the measurement protocol, see Table S2A. CAM = central age model; OD = overdispersion (Galbraith & Roberts 2012).

Sample	Depth below surface (m)	Radionuclide concentration			Water content (%)	Total dose rate (Gy ka^{-1})	CAM D_e (Gy)	Number of aliquots	OD (%)	Age (ka)
		U (ppm)	Th (ppm)	K (%)						
ARP01	0.15	3.4±0.2	10.5±0.5	1.6±0.1	18	3.53±0.13	14.51±0.45	11	8.6	4.1±0.2
ARP02	0.15	3.4±0.2	10.5±0.5	1.6±0.1	18	3.53±0.13	8.14±0.36	12	14.7	2.3±0.1
CRE01	2.35	3.2±0.2	12.0±0.6	1.8±0.1	28	3.36±0.12	33.45±1.51	12	15.1	10.0±0.6
CRE02	2.65	3.4±0.3	11.7±0.6	1.8±0.1	27	3.40±0.13	41.90±1.78	12	14.0	12.3±0.7
CRE03	3.17	2.9±0.2	10.4±0.5	1.6±0.1	33	2.89±0.10	78.44±1.71	12	4.5	27.2±1.1
CRE04	3.73	3.1±0.2	10.3±0.5	1.8±0.1	31	3.08±0.11	28.18±1.38	7	8.9	9.1±0.6

et al. 2015) for the ARP aeolian material. Further geochemical analyses would be necessary (Újvári *et al.* 2015) to quantitatively discuss the origin of such aeolian sediments in the context of atmospheric palaeo-circulations at the scale of the European Alps (e.g. Muhs *et al.* 2014; Rousseau *et al.* 2006).

Conventional luminescence dating on ARP silty sediments provides ages ranging between 2 and 7 ka, with an observed discrepancy between OSL and IRSL ages and no clear systematic trend (Fig. 9, Tables 1, 2). This mismatch is further highlighted by portable luminescence measurements, with different patterns in OSL and IRSL intensity profiles (i.e. higher OSL variability compared to depth-increasing IRSL signal; Fig. 9). Different luminescence signal resetting rates under light exposure (i.e. bleaching) have been reported in the literature (Murray *et al.* 2012), with quartz OSL signal bleaching more rapidly than feldspar IRSL. Our observations can be explained by (i) partial bleaching of the ARP silt before deposition, which would lead to overestimation of the true depositional age, and/or (ii) differential post-depositional bleaching through cryoturbation, which would cause underestimation of the true depositional age. Based on the sedimentology, we favour the post-depositional bleaching hypothesis: there is high probability that the ARP silt was completely bleached prior to deposition, since aeolian sediment transport is commonly associated with efficient sunlight exposure (Li & Wintle 1992). After deposition, active cryoturbation processes resulted in both sediment reworking and formation of the overlying patterned ground (unit 1; Fig. 4). Frost and thaw processes have continually mobilized sediment patches from various depths (Bertran *et al.* 2019), causing light exposure of reworked sediments and the (partial) resetting of their luminescence signal. Similarly, stratigraphical inconsistency and large variability in luminescence ages have been observed for periglacial sediment deposits, and have been attributed to post-depositional reworking due to active cryoturbation processes (Bateman 2008; Andrieux *et al.* 2018). Our young OSL (2.3–4.1 ka) and IRSL (2.5–2.8 ka) ages are therefore probably the result of recent/ongoing post-depositional bleaching through periglacial sediment reworking, while the IRSL age of sample ARP02 (7.1±0.7 ka) is interpreted as a minimum age for the high-elevation aeolian deposit. This minimum age estimate is in agreement with low-elevation loess from the Rhône Valley attributed to the late YD/Early Holocene, based on luminescence dating (Guélat 2013; Parriaux *et al.* 2017).

To summarize, the high-elevation ARP deposit reflects Lateglacial to Holocene aeolian dynamics in the Sanetsch area, in line with previous aeolian sediment reconstructions in the Swiss Alps and foreland (Pochon 1973; Guélat 2013; Martignier *et al.* 2015). The ARP primary aeolian deposit presents a mixed autochthonous (bedrock and moraine-deposit deflation) and allochthonous (nearby alluvial plains such as the Rhône Valley) origin. Luminescence dating suggests that deposition occurred at least *c.* 7 ka ago; however, this only remains a minimum age estimate due to recent/ongoing active cryoturbation and sediment reworking at the ARP site. The ARP aeolian deposit may give also insights into the presence of high-elevation ice-free areas (nunataks) in the Alps already during the LGM or the early Lateglacial (Bini *et al.* 2009; Martignier *et al.* 2015; Gild *et al.* 2018), where aeolian sediment could accumulate, in proximity to glacially covered areas. Furthermore, luminescence

Table 2. Sample luminescence details and corresponding polymineral IRSL dating results. See Table 1 (ARP samples) for radionuclide concentration and water content. For analytical details about the measurement protocol, see Table S2B. CAM = central age model; OD = overdispersion (Galbraith & Roberts 2012).

Sample	Depth below surface (m)	Total dose rate (Gy ka^{-1})	CAM uncorrected D_e (Gy)	Number of aliquots	OD (%)	$g_{2\ \text{days}}$ (% per decade)	CAM corrected D_e (Gy)	Age (ka)
ARP01	0.15	4.13±0.15	10.57±0.35	11	0	1.26±1.03	11.77±1.21	2.8±0.3
ARP02	0.15	4.13±0.15	26.01±1.02	10	9.82	1.39±0.88	29.50±2.88	7.1±0.7
ARP03	0.15	4.13±0.15	9.02±0.47	12	14.47	1.43±0.98	10.19±1.08	2.5±0.3

Table 3. Details on cosmogenic ^{10}Be samples, concentrations and exposure ages. Sample thickness and density are 2.5 cm and 2.65 g cm^{-3}, respectively.

Sample	Location WGS 84 (°N/°E)	Elevation (m a.s.l.)	Topographic shielding[1]	^{10}Be/^{9}Be blank corrected (10^{-13} at g^{-1})	^{10}Be/^{9}Be uncertainty (%)	^{10}Be concentration (10^{5} at g^{-1})	^{10}Be exposure age (ka)[2]	
							No snow/ erosion	Incl. snow/ erosion[3]
SAN18_01	46.35111/7.28751	2055	0.92	1.46	3.33	1.86±0.06	9.3±0.4	10.1±0.4
SAN18_02	46.35117/7.28900	2056	0.96	1.55	3.38	1.96±0.07	9.4±0.4	10.1±0.4
SAN18_03	46.35137/7.28874	2054	0.94	1.76	3.39	2.01±0.07	9.8±0.4	10.6±0.4

[1] Topographic shielding correction according to Dunne *et al.* (1999).

[2] ^{10}Be production rate of 4.16±0.10 at g^{-1} a^{-1} (Claude *et al.* 2014) and LSDn scaling scheme (Lifton *et al.* 2014).

[3] 50 cm snow cover for 6 months per year (Wirsig *et al.* 2016a), snow density of 0.3 g cm^{-3} and spallation attenuation length in snow of 109 g cm^{-2} (Delunel *et al.* 2014). Erosion rate of 1 mm ka^{-1} (Wirsig *et al.* 2016a, b).

analyses (both portable and conventional dating) have highlighted the occurrence of (ongoing) cryoturbation processes at the ARP site, providing a potential palaeoclimatic proxy for the Holocene but requiring further investigation (e.g. Vandenberghe 2013; Rousseau *et al.* 2006).

Alluvial fan (CRE site) – Insights into the depositional history of the CRE alluvial fan and its connection to the surrounding landforms and deposits also emerge from our multi-method results. XRD and micromorphological analyses confirm field stratigraphical observations (Table S4), revealing a local bedrock origin for the clasts contained in the heterogeneous and gravel layers of the fan (Figs 5, 7, 8). This is suggested by the moderate calcite content (5–39%; Fig. 8) in most of the heterogeneous CRE units, which likely relates to the presence of bedrock-derived weathered granules and pebbles (55–66% calcite content in both siliceous limestone and calcareous shales; Fig. 8). The absence of calcite in some heterogeneous layers can be explained by clast weathering and complete decarbonation as observed in the field (very little/no reaction to HCl; Table S4). Thin section analyses further highlight mineralogical and grain-size similarities between weathered clasts and bedrock (Fig. 7C, D), with abundant quartz grains of similar sizes (10–150 μm) in both bedrock and clasts. The absence of a developed weathering cortex around the clasts suggests that weathering did not occur *in situ* (i.e. after clast deposition in the alluvial fan), but is probably inherited from a previous alteration phase (e.g. within morainic and/ or slope parental deposits). Further support for this hypothesis is given by the low TOC along the fan stratigraphy, which implies absence of palaeo-soils and therefore little *in situ* weathering by pedogenesis.

Field stratigraphical observations and grain size and XRD analyses also show similarities between the fine/ heterogeneous CRE layers and the high-elevation ARP deposit. Grain-size distributions closely overlap for CRE and ARP samples (G1 to G6, and G7 and G8, respectively; Fig. 6), with multiple modes (4–8, 35 and 150 μm), good sorting (2.7–3.3) and silty fraction dominance (D_{50} between 10.9 and 16.5 μm). Mineralogical analyses further support this observation, with the absence of calcite (except for CRE15, which probably integrates clasts from overlying/underlying gravel units) and the dominance of quartz (40–54%) and micas (23–43%). Stratigraphy and micromorphological analyses also show (i) fining-up sedimentary sequences within some CRE units (i.e. from weathered calcareous granules and pebbles at the base to silty loam at the top; Fig. 5, Table S4), (ii) a moderately developed subangular blocky microstructure (unit 6; Fig. 7A) and (iii) well-developed 1 to 5 mm thick horizontal laminae (units 7 and 13; Fig. 7B). All together, these observations point towards an alluvial reworking of aeolian sediments to form the fine units and the matrix of the heterogeneous units of the CRE alluvial fan. Deposition of reworked aeolian sediments could have occurred in a lake, or possibly in a pond within the alluvial fan, as suggested by the fining-up sedimentary sequences (units 3, 4 and 5) and the horizontal laminae (units 7 and 13). Isolated pebbles and cobbles (fine units 7, 9 and 10) can be interpreted as possible dropstones, and would support the lake hypothesis. Based on the presence of slickensides and mottling (unit 6; Fig. 7A) as well as Fe-Mn precipitation, we hypothesize ephemeral lake/pond conditions with wetting/drying cycles and low-sedimentation phases, during which the original depositional microstructure (Fig. 7B) was destroyed.

Luminescence measurements (both portable and conventional OSL), show a general alternating pattern between two populations of low counts/young ages and high counts/old ages along the fan stratigraphy (Fig. 10). We propose that these OSL trends reflect differences in quartz provenance as well as transport processes. For the heterogeneous layers, we expect the high OSL counts and old OSL age to result from the mixing and signal-averaging between grains from weathered clasts carrying an inherited signal (i.e. no light exposure during transport) with well-bleached grains (i.e. full luminescence

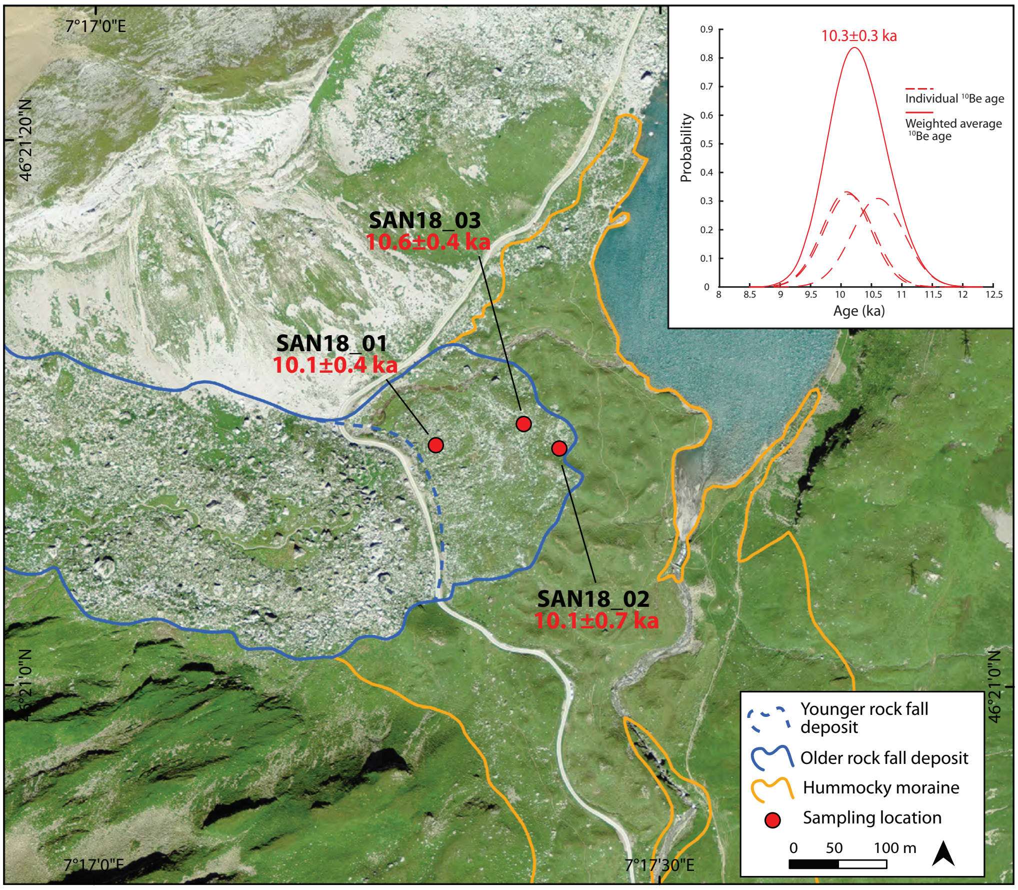

Fig. 11. ^{10}Be surface exposure ages from rockfall sandstone boulders lying on the hummocky moraine (SAN site, modified orthophoto from swisstopo, authorization 5701367467/000010). ^{10}Be surface exposure ages calculated with snow and erosion corrections are shown. See Table 3 for the ages obtained without applying any correction. The blue dashed line delimits the extent of a younger rockfall deposit than the one dated in the present study. Inset shows probability density plots of the individual and weighted-average ^{10}Be surface exposure ages, after snow and erosion corrections.

signal reset prior to deposition) coming from reworked aeolian material. Moreover, sediments from heterogeneous units were probably transported and deposited during periods of high-sediment supply by sheetflow events: transportation in dense and turbid flows could have prevented the complete OSL bleaching of reworked quartz grains, leading therefore to higher luminescence counts and overestimated OSL age (i.e. CRE03 at 27.2±1.1 ka). Fine layers, characterized by low OSL counts and young OSL ages, may have settled during periods of lower sediment supply by decantation in water, allowing complete/better OSL bleaching prior to deposition. We therefore interpret OSL ages of the fine CRE units (CRE01, 02 and 04; weighted-average age of 10.5±1.6 ka) as more representative of the true depositional age of the CRE alluvial fan. Potential incorporation of lithic fragments could explain the slightly older OSL age for sample CRE02 (12.3±1.6 ka, unit 6). In summary, CRE fan deposition most likely occurred during or soon after the YD. This proposed chronology agrees with the onset of sedimentation in Pond Emine (Fig. 2) at *c.* 12 ka ago (Berthel *et al.* 2012; Steinemann *et al.* 2020), implying that the Sanetsch Pass and the alluvial plain were ice-free during (or soon after) the YD, and that the subsequent sediment connectivity and transport from the hillslopes towards the plain (CRE site) established quickly.

Hummocky moraine and rockfall boulders (SAN site) – The average ^{10}Be surface exposure age from the three rockfall boulders is 10.3±0.3 or 9.5±0.2 ka, calculated respectively with or without erosion and snow corrections. For the rest of the discussion, we focus on the age estimate obtained with erosion (1 mm ka^{-1}; Wirsig *et al.* 2016b) and snow corrections (50-cm snow thickness over 6 months per year; based on Wirsig *et al.* 2016b and our own field observations). We, however, note that the uncorrected age estimate differs by <10%, and would not lead to any significant change in our proposed geomorphological reconstruction.

Dating of the rockfall boulders (*c.* 10 ka; Fig. 11) provides a minimum age constraint for the hummocky moraine formation, which occurred before or at the time of the rockfall event. Based on field observations of boulder distribution, we propose a scenario where the rockfall occurred over stagnant ice. If the rockfall had occurred when the hummocky moraine was already formed, the boulders would have been deposited mainly in the intra-hummock hollows, due to gravity. Instead, the uniform distribution of rockfall boulders, placed both on hummock ridges and in intra-hummock hollows, suggests that the rockfall spread over a disconnected ice body, before or during the formation of the underlying hummocky morphology. We further hypothesize that this stagnant ice body could have temporarily dammed an ephemeral lake in the plain, where the CRE alluvial fan was deposited around 10 ka ago.

At a regional scale, this rockfall event is contemporaneous with several other Early Holocene gravitational events reported within the Alps (10–9 ka; Ivy-Ochs *et al.* 2017 and reference therein), including two coeval landslides of the Rinderhorn region (Bernese Alps, Switzerland; Grämiger *et al.* 2016), at only 28-km distance from the Sanetsch Pass. Glacial debuttressing (Cossart *et al.* 2008) and rock stress changes associated with repeated glacial fluctuations (Grämiger *et al.* 2017) were probably the trigger mechanisms behind the rockslope failure.

The rockfall event investigated here was probably followed by a second event, characterized by smaller extent (Fig. 11). Age constraint for this subsequent event is, however, not available, but may be related to Holocene landslide/rockslide clusters observed elsewhere in the European Alps (Zerathe *et al.* 2014; Ivy-Ochs *et al.* 2017).

Lateglacial to Holocene palaeoenvironmental reconstruction

By combining our field observations and multi-method results, we propose a palaeoenvironmental reconstruction of the Sanetsch Pass area during the Lateglacial–Holocene transition, with the aim to highlight the interplay between different sedimentary and geomorphic processes (Fig. 12).

Throughout the LGM and Lateglacial periods, the area north of Sanetsch Pass was ice-covered, while some peaks were protruding above the ice surface (nunataks, Fig. 12A; Bini *et al.* 2009), similar to the overall European Alps. These conditions may have favoured deposition of aeolian drapes on nunatak platforms already at this time (Gild *et al.* 2018), with an allochthonous contribution of the wind-blown material as confirmed by XRD analyses (ARP site), although local vs. more distal sources cannot be discriminated by our multi-method approach and would require further investigations. Lateral morainic ridges and glacial deposits in the Sanetsch plain (Fig. 2) do not have tight chronological constraints but they are likely related to ice retreat stadials during the Lateglacial (Ivy-Ochs *et al.* 2007). Several indications point towards an onset of glacier retreat for the Sanetsch Pass and our investigated area at the end of the YD (Fig. 12B), in close agreement with other palaeoglacial and lacustrine chronologies in the Swiss Alps (Schwander *et al.* 2000; Heiri *et al.* 2014; Schimmelpfennig *et al.* 2014). The Pond Emines (Fig. 2) became ice-free during the same time period (*c.* 12 ka; Berthel *et al.* 2012), when the Tsanfleuron glacier finally retreated close to the most external LIA morainic ridges (~1 km west of the Sanetsch Pass; Fig. 2), similar to other palaeoglaciological reconstructions in the Alps (Schimmelpfennig *et al.* 2012; Kronig *et al.* 2018). A disconnected ice body, thick and sediment-rich, persisted at the downstream end of the Sanetsch plain until *c.* 10 ka and formed a hummocky morphology overridden by rockfall deposits.

Glacier retreat in the Sanetsch Pass area was associated with rapid (re-)establishment of paraglacial and periglacial geomorphic processes, promoting sediment connectivity and transport and resulting in major landscape changes. All these processes illustrate and synthesize postglacial alpine dynamics (Church & Ryder 1972; Mercier & Etienne 2008; Fig. 12B), as summarized below. Firstly, ice retreat promoted slope processes, as well as aeolian remobilization of glacially -derived erosion products. Fine sediments in glacial outwash plains, within the Sanetsch Pass area or other nearby valleys (e.g. the Rhône Valley), were probably entrained and redeposited on mountain flanks and low-relief areas by local katabatic winds and/or regional winds (Bullard & Austin 2011; Martignier *et al.* 2015). Post-YD paraglacial relaxation favoured hillslope dynamics and sediment entrainment (Sanders & Ostermann 2011), with catastrophic rockfall events such as the rockslope failure of Les Montons cliff (Figs 3, 11; Ivy-Ochs *et al.* 2017). The alluvial fan (CRE site) was deposited at the downstream end of the fluvioglacial plain, probably within an ephemeral ice-dammed lake contemporary to the hummocky moraine formation. Exposed catchment-slope deposits (i.e. aeolian, glacial and talus) were remobilized and transported downhill into the plain, where they were redeposited to form a stratigraphical succession of coarse and fine layers within the CRE alluvial fan (Beaudoin & King 1994). We propose that the aeolian deposit identified on the high-elevation plateau (ARP site) is a remnant of a broader aeolian drape. The ARP aeolian sediments have been preserved due to the low connectivity between the platform and the downstream hillslopes (Figs 2, 3), but this potentially more-extensive deposit has been eroded elsewhere in the Sanetsch Pass area, with the reworked fine sediments being eventually incorporated in the alluvial fan downslope.

Based on our OSL chronology, we hypothesize that short-lived sedimentation in the CRE alluvial fan stopped or slowed down already during/soon after the YD, resulting from a drastic change in base-level and

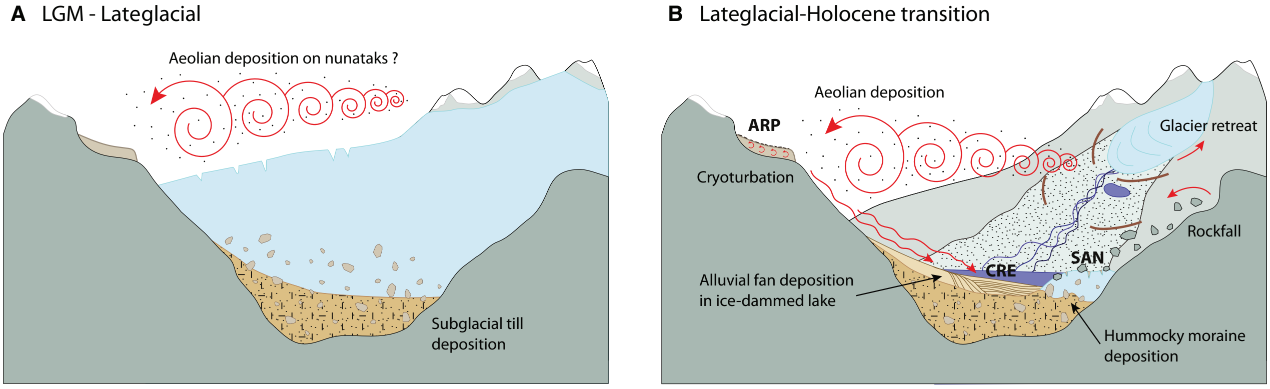

Fig. 12. Schematic palaeoenvironmental reconstruction of the study area. A. Glacier extent with subglacial sediment deposition, and aeolian drapes deposition on nunatak platforms, during the LGM and Lateglacial periods. B. Paraglacial (alluvial, colluvial, lacustrine, aeolian) and periglacial (cryoturbation) geomorphic processes during/soon after glacier retreat, at the Lateglacial–Holocene transition. The three landforms investigated in the study are indicated (ARP, CRE, SAN).

sedimentation dynamics due to the melting of the ice-dam. Since then, landscape dynamics around the Sanetsch Pass seem to have been dominated by (i) hillslope denudation (Hendrickx *et al.* in press) and localized stream incision within bedrock and glacial/alluvial sediments (Figs 2, 3C) at low elevations, and (ii) active periglacial processes at high elevations, with aeolian sediment cryoturbation (ARP site) and rock glaciers within scree deposits (Fig. 2).

Conclusions

Based on a combined approach of geomorphological and sedimentological field investigations together with different analytical methods, we proposed a detailed reconstruction of post-LGM palaeoenvironmental conditions and geomorphic connectivity in the Sanetsch Pass area (western Swiss Alps). Our study provides quantitative constraints for the high-altitude landscape response to ice retreat and climate changes during the Lateglacial–Holocene transition. Our multi-method results show that silty sediments from the high-elevation platform are primary aeolian sediments, deposited on ice-free areas before or during the post-YD glacier retreat and then reworked by cryoturbation. Post-YD ice retreat was also associated with slope relaxation and aeolian/glacial sediment remobilization. This is evidenced by the contemporary occurrence of hummocky moraine formation, rockfall event and alluvial fan deposition within an ephemeral ice-dammed lake, all taking place at *c.* 10–12 ka. Altogether, our results highlight the development of rapid and most probably transient landscape changes in high Alpine regions during the Lateglacial–Holocene transition, with an increase in sediment flux following glacier retreat and the establishment of paraglacial and periglacial geomorphic processes.

Several palaeoclimatic archives, mainly from lacustrine and peat records, have documented the pronounced climatic and environmental change associated with the end of the YD in the European Alps. In this study, we have shown that landscape dynamics and connectivity between geomorphic markers can also be used as quantitative proxies to constrain the environmental response to this climatic transition.

Acknowledgements. – The authors thank M. Gobat for sharing his intuition of a possible aeolian deposit on the Arpille plateau, and N. Diaz, P. Pérez Cutillas and B. Lehmann for help during field investigations. S. Lane (University of Lausanne) is warmly thanked for access to the portable luminescence reader. P. Renzel and T. Beckmann are thanked for the grain-size analyses and micromorphological thin section preparation. M. Guélat is thanked for sharing unpublished mineralogical and grain-size data from aeolian deposits of the Rhône Valley. J. Krbanjevic is thanked for support during geochemistry analyses. The authors warmly thank the ASTER team (D. Bourlès, G. Aumaitre, K. Keddadouche and R. Braucher) for the measurements performed at the ASTER AMS facility (CEREGE, Aix-en-Provence). I. Schimmelpfening, one anonymous reviewer and the editor J.A. Piotrowski are thanked for constructive reviews and manuscript corrections. This study was supported by the Swiss National Science Foundation SNSF (Grant PP00P2_170559) and the French ANR-PIA programme (ANR-18-MPGA-0006). All data are available in tables in the main text and online supporting information.

Author contributions. – LB, PGV and RD designed the study. ES, LB, PGV and RD performed field investigations and sample collection. ES performed luminescence analysis (with NG and PGV), grain-size and micromorphology analysis (with LB), XRD analysis (with BG) and ^{10}Be cosmogenic analysis (with JC and PGV). ES wrote the manuscript with input from all co-authors.

References

Aitken, M. J. 1985: Thermoluminescence dating: past progress and future trends. *Nuclear Tracks and Radiation Measurements (1982) 10*, 3–6.

Andrieux, E., Bateman, M. D. & Bertran, P. 2018: The chronology of Late Pleistocene thermal contraction cracking derived from sand wedge OSL dating in central and southern France. *Global and Planetary Change 162*, 84–100.

Arnold, M., Merchel, S., Bourlès, D. L., Braucher, R., Benedetti, L., Finkel, R. C., Aumaître, G., Gottdang, A. & Klein, M. 2010: The

French accelerator mass spectrometry facility ASTER: improved performance and developments. *Nuclear Instruments and Methods in Physics Research Section B: Beam Interactions with Materials and Atoms 268*, 1954–1959.

Auclair, M., Lamothe, M. & Huot, S. 2003: Measurement of anomalous fading for feldspar IRSL using SAR. *Radiation Measurements 37*, 487–492.

Badoux, H., Bonnard, E. G., Burri, M. & Vischer, A. 1959: *Map sheet 1286 St-Léonard with explanatory note 35. Swiss Geological Atlas 1:25,000*. Service hydrologique et géologique national, Berne.

Ballantyne, C. K. 2002: Paraglacial geomorphology. *Quaternary Science Reviews 21*, 1935–2017.

Bateman, M. D. 2008: Luminescence dating of periglacial sediments and structures. *Boreas 37*, 574–588.

Beaudoin, A. B. & King, R. H. 1994: Holocene palaeoenvironmental record preserved in a paraglacial alluvial fan, Sunwapta Pass, Jasper National Park, Alberta, Canada. *Catena 22*, 227–248.

Benn, D. I. & Evans, D. J. A. 2014: *Glaciers and Glaciation*. 568 pp. Routledge, London.

Berthel, N., Schwörer, C. & Tinner, W. 2012: Impact of Holocene climate changes on alpine and treeline vegetation at Sanetsch Pass, Bernese Alps, Switzerland. *Review of Palaeobotany and Palynology 174*, 91–100.

Bertran, P., Font, M., Giret, A., Manchuel, K. & Sicilia, D. 2019: Experimental soft-sediment deformation caused by fluidization and intrusive ice melt in sand. *Sedimentology 66*, 1102–1117.

Bini, A., Buoncristiani, J., Couterrand, S. & Ellwanger, D. 2009: *Switzerland during the Last Glacial Maximum (LGM) 1:500,000*. Federal Office of Topography, Swisstopo.

Borgatti, L. & Soldati, M. 2010: Landslides as a geomorphological proxy for climate change: a record from the Dolomites (northern Italy). *Geomorphology 120*, 56–64.

Braucher, R., Guillou, V., Bourles, D. L., Arnold, M., Aumaitre, G., Keddadouche, K. & Nottoli, E. 2015: Preparation of ASTER in-house ^{10}Be/^{9}Be standard solutions. *Nuclear Instruments and Methods in Physics Research Section B: Beam Interactions with Materials and Atoms 361*, 335–340.

Brown, E. T., Edmond, J. M., Raisbeck, G. M., Yiou, F., Kurz, M. D. & Brook, E. J. 1991: Examination of surface exposure ages of Antarctic moraines using in situ produced ^{10}Be and ^{26}Al. *Geochimica et Cosmochimica Acta 55*, 2269–2283.

Bullard, J. E. & Austin, M. J. 2011: Dust generation on a proglacial floodplain, West Greenland. *Aeolian Research 3*, 43–54.

Buylaert, J. P., Murray, A. S., Thomsen, K. J. & Jain, M. 2009: Testing the potential of an elevated temperature IRSL signal from K-feldspar. *Radiation Measurements 44*, 560–565.

Church, M. & Ryder, J. M. 1972: Paraglacial sedimentation: a consideration of fluvial processes conditioned by glaciation. *Bulletin of the Geological Society of America 83*, 3059–3072.

Clark, P. U., Dyke, A. S., Shakun, J. D., Carlson, A. E., Clark, J., Wohlfarth, B., Mitrovica, J. X., Hostetler, S. W. & McCabe, A. M. 2009: The Last Glacial Maximum. *Science 325*, 710–714.

Claude, A., Ivy-Ochs, S., Kober, F., Antognini, M., Salcher, B. & Kubik, P. W. 2014: The Chironico landslide (Valle Leventina, southern Swiss Alps): age and evolution. *Swiss Journal of Geosciences 107*, 273–291.

Colombo, N., Paro, L., Godone, D. & Fratianni, S. 2016: Geomorphology of the Hohsand basin (Western Italian Alps). *Journal of Maps 12*, 975–978.

Cossart, E., Braucher, R., Fort, M., Bourlès, D. L. & Carcaillet, J. 2008: Slope instability in relation to glacial debuttressing in alpine areas (Upper Durance catchment, southeastern France): evidence from field data and ^{10}Be cosmic ray exposure ages. *Geomorphology 95*, 3–26.

Cossart, E., Mercier, D., Decaulne, A. & Feuillet, T. 2013: An overview of the consequences of paraglacial landsliding on deglaciated mountain slopes: typology, timing and contribution to cascading fluxes. *Quaternaire 24*, 13–24.

Delunel, R., Bourlès, D. L., van der Beek, P. A., Schlunegger, F., Leya, I., Masarik, J. & Paquet, E. 2014: Snow shielding factors for cosmogenic nuclide dating inferred from long-term neutron detector monitoring. *Quaternary Geochronology 24*, 16–26.

Dunne, J., Elmore, D. & Muzikar, P. 1999: Scaling factors for the rates of production of cosmogenic nuclides for geometric shielding and attenuation at depth on sloped surfaces. *Geomorphology 27*, 3–11.

Durcan, J. A., King, G. E. & Duller, G. A. T. 2015: DRAC: Dose Rate and Age Calculator for trapped charge dating. *Quaternary Geochronology 28*, 54–61.

Ehlers, J. & Gibbard, P. 2004: *Quaternary Glaciations-Extent and Chronology: Part I: Europe*. 488 pp. Elsevier, Amsterdam.

Föllmi, K. B., Bodin, S., Godet, A., Linder, P. & van de Schootbrugge, B. 2007: Unlocking paleo-environmental information from Early Cretaceous shelf sediments in the Helvetic Alps: stratigraphy is the key! *Swiss Journal of Geosciences 100*, 349–369.

French, H. M. 2007: *The Periglacial Environment*. 151 pp. John Wiley & Sons, Chichester.

Galbraith, R. F. & Roberts, R. G. 2012: Statistical aspects of equivalent dose and error calculation and display in OSL dating: an overview and some recommendations. *Quaternary Geochronology 11*, 1–27.

Geilhausen, M., Morche, D., Otto, J.-C. & Schrott, L. 2013: Sediment discharge from the proglacial zone of a retreating Alpine glacier. *Zeitschrift für Geomorphologie, Supplementary Issues 57*, 29–53.

Gild, C., Geitner, C. & Sanders, D. 2018: Discovery of a landscape-wide drape of Lateglacial aeolian silt in the western Northern Calcareous Alps (Austria): first results and implications. *Geomorphology 301*, 39–52.

Gobat, J. & Guenat, C. 2019: *Sols et paysages. Types de sols, fonctions et usages en Europe moyenne*. 169 pp. PPUR, Lausanne.

Gosse, J. C. & Phillips, F. M. 2001: Terrestrial in situ cosmogenic nuclides: theory and application. *Quaternary Science Reviews 20*, 1475–1560.

Grämiger, L. M., Moore, J. R., Gischig, V. S., Ivy-Ochs, S. & Loew, S. 2017: Beyond debuttressing: mechanics of paraglacial rock slope damage during repeat glacial cycles. *Journal of Geophysical Research: Earth Surface 122*, 1004–1036.

Grämiger, L. M., Moore, J. R., Vockenhuber, C., Aaron, J., Hajdas, I. & Ivy-Ochs, S. 2016: Two early Holocene rock avalanches in the Bernese Alps (Rinderhorn, Switzerland). *Geomorphology 268*, 207–221.

Guélat, M. 2013: Les Loess de la Vallée du Rhône. *Bulletin de la Murithienne 131*, p. 109.

Hadjouis, A. 1987: Granulométrie des fractions sableuses. *In* Miskovsky, J-C (ed.): *Géologie de la péehistoire: méthodes, techniques, applications*, 413–426. Association pour l'étude de l'environnement géologique de la préhistoire (AEEGP), Paris.

Hanspeter, H., Michel, M. & Heinz, Z. 2005: Glacier and lake-level variations in west-central Europe over the last 3500 years. *The Holocene 6*, 789–801.

Hantke, R. 1992: *Eiszeitalter - Die jüngste Erdgeschichte der Alpen und ihrer Nachbargebiete*. 468, 703 and 730 pp. Ecomed-Verlag, Landsberg/Lech.

Hendrickx, H., De Sloover, L., Stal, C., Delaloye, R., Nyssen, J., Frankl, A. in press: Talus slope geomorphology investigated at multiple time scales from high-resolution topographic surveys and historical aerial photographs (Sanetsch Pass, Switzerland). *Earth Surfurface Processes and Landforms*. https://doi.org/10.1002/esp.4989

Heiri, O., Koinig, K. A., Spötl, C., Barrett, S., Brauer, A., Drescher-Schneider, R., Gaar, D., Ivy-Ochs, S., Kerschner, H., Luetscher, M., Moran, A., Nicolussi, K., Preusser, F., Schmidt, R., Schoeneich, P., Schwörer, C., Sprafke, T., Terhorst, B. & Tinner, W. 2014: Palaeoclimate records 60-8 ka in the Austrian and Swiss Alps and their forelands. *Quaternary Science Reviews 106*, 186–205.

Hinderer, M. 2001: Late Quaternary denudation of the Alps, valley and lake fillings and modern river loads. *Geodinamica Acta 14*, 231–263.

Hippe, K., Ivy-Ochs, S., Kober, F., Zasadni, J., Wieler, R., Wacker, L., Kubik, P. W. & Schlüchter, C. 2014: Chronology of Lateglacial ice flow reorganization and deglaciation in the Gotthard Pass area, Central Swiss Alps, based on cosmogenic ^{10}Be and in situ ^{14}C. *Quaternary Geochronology 19*, 14–26.

Huntley, D. J. & Lamothe, M. 2011: Ubiquity of anomalous fading in K-feldspars and the measurement and correction for it in optical dating. *Canadian Journal of Earth Sciences 38*, 1093–1106.

Ivy-Ochs, S. 2015: Glacier variations in the European Alps at the end of the last glaciation. *Cuadernos de Investigación Geográfica 41*, 295–315.

Ivy-Ochs, S., Kerschner, H., Maisch, M., Christl, M., Kubik, P. W. & Schlüchter, C. 2009: Latest Pleistocene and Holocene glacier variations in the European Alps. *Quaternary Science Reviews 28*, 2137–2149.

Ivy-Ochs, S., Kerschner, H. & Schlüchter, C. 2007: Cosmogenic nuclides and the dating of Lateglacial and Early Holocene glacier variations: the Alpine perspective. *Quaternary International 164–165*, 53–63.

Ivy-Ochs, S., Martin, S., Campedel, P., Hippe, K., Alfimov, V., Vockenhuber, C., Andreotti, E., Carugati, G., Pasqual, D., Rigo, M. & Viganò, A. 2017: Geomorphology and age of the Marocche di Dro rock avalanches (Trentino, Italy). *Quaternary Science Reviews 169*, 188–205.

Ivy-Ochs, S., Schäfer, J., Kubik, P. W., Synal, H. A. & Schlüchter, C. 2004: Timing of deglaciation on the northern Alpine foreland (Switzerland). *Eclogae Geologicae Helvetiae 97*, 47–55.

King, G. E., Sanderson, D. C. W., Robinson, R. A. J. & Finch, A. A. 2014: Understanding processes of sediment bleaching in glacial settings using a portable OSL reader. *Boreas 43*, 955–972.

Korup, O. & Schlunegger, F. 2007: Bedrock landsliding, river incision, and transience of geomorphic hillslope-channel coupling: evidence from inner gorges in the Swiss Alps. *Journal of Geophysical Research: Earth Surface 112*, F03027, https://doi.org/10.1029/2006jf000710.

Kreutzer, S., Schmidt, C., Fuchs, M. & Dietze, M. 2012: Introducing an R package for luminescence dating analysis. *Ancient TL 30*, 1–8.

Kronig, O., Ivy-Ochs, S., Hajdas, I., Christl, M., Wirsig, C. & Schlüchter, C. 2018: Holocene evolution of the Triftje- and the Oberseegletscher (Swiss Alps) constrained with ^{10}Be exposure and radiocarbon dating. *Swiss Journal of Geosciences 111*, 117–131.

Li, S. H. & Wintle, A. G. 1992: Luminescence sensitivity change due to bleaching of sediments. *International Journal of Radiation Applications and Instrumentation. Part 20*, 567–573.

Lifton, N. 2016: Implications of two Holocene time-dependent geomagnetic models for cosmogenic nuclide production rate scaling. *Earth and Planetary Science Letters 433*, 257–268.

Lifton, N., Sato, T. & Dunai, T. J. 2014: Scaling in situ cosmogenic nuclide production rates using analytical approximations to atmospheric cosmic-ray fluxes. *Earth and Planetary Science Letters 386*, 149–160.

Lowick, S. E., Buechi, M. W., Gaar, D., Graf, H. R. & Preusser, F. 2015: Luminescence dating of Middle Pleistocene proglacial deposits from northern Switzerland: methodological aspects and stratigraphical conclusions. *Boreas 44*, 459–482.

Martignier, L., Nussbaumer, M., Adatte, T., Gobat, J. M. & Verrecchia, E. P. 2015: Assessment of a locally-sourced loess system in Europe: The Swiss Jura Mountains. *Aeolian Research 18*, 11–21.

Martin, L. C. P., Blard, P.- H., Balco, G., Lavé, J., Delunel, R., Lifton, N. & Laurent, V. 2017: The CREp program and the ICE-D production rate calibration database: a fully parameterizable and updated online tool to compute cosmic-ray exposure ages. *Quaternary Geochronology 38*, 25–49.

Masson, H., Herb, R. & Steck, A. 1980: Helvetic Alps of Western Switzerland. Trumpy, R. (ed.): *Geology of Switzerland, a Guide Book (Part B)*, 109–153. Birkhäuserverlag, Basel.

Menkveld-Gfeller, U. 1997: Die Bürgen-Fm. und die Klimsenhorn-Fm.: Formelle Definition zweier lithostratigraphischer Einheiten des Eozäns der helvetischen Decken. *Eclogae Geologicae Helvetiae 90*, 245–261.

Merchel, S. & Herpers, U. 1999: An update on radiochemical separation techniques for the determination of long-lived radionuclides via accelerator mass spectrometry. *Radiochimica Acta 84*, 215–220.

Mercier, D. & Etienne, S. 2008: Paraglacial geomorphology: processes and paraglacial context. *Geomorphology 95*, 1–102.

Muhs, D. R. 2013: Loess and its geomorphic, stratigraphic, and paleoclimatic significance in the Quaternary. *Treatise on Geomorphology 11*, 149–183.

Muhs, D. R., Cattle, S. R., Crouvi, O., Rousseau, D. D., Sun, J. & Zárate, M. A. 2014: Loess record. *In* Knippertz, P. & Stuut, J.-B. (eds.): *Mineral Dust: A Key Player in the Earth System*, 411–441. Springer, Dordrecht.

Muñoz-Salinas, E., Bishop, P., Sanderson, D. & Kinnaird, T. 2014: Using OSL to assess hypotheses related to the impacts of land use change with the early nineteenth century arrival of Europeans in southeastern Australia: an exploratory case study from Grabben Gullen Creek, New South Wales. *Earth Surface Processes and Landforms 39*, 1576–1586.

Murray, A. S. & Wintle, A. G. 2000: Dating quartz using an improved single-aliquot regenerative-dose (SAR) protocol. *Radiation Measurements 32*, 57–73.

Murray, A. S., Thomsen, K. J., Masuda, N., Buylaert, J. P. & Jain, M. 2012: Identifying well-bleached quartz using the different bleaching rates of quartz and feldspar luminescence signals. *Radiation Measurements 47*, 688–695.

Nelson, M. S., Gray, H. J., Johnson, J. A., Rittenour, T. M., Feathers, J. K. & Mahan, S. A. 2015: User guide for luminescence sampling in archaeological and geological contexts. *Advances in Archaeological Practice 3*, 166–177.

Parriaux, A., Burri, M. & Weidmann, M. 2017: Données nouvelles sur la géologie des collines de Chiètres. *Bulletin de la Société vaudoise des sciences naturelles 96*, 31–48.

Pochon, M. 1973: Apport allochtone dans les sols jurassiens (Jura vaudois et Jura neuchâtelois). *Bulletin de la Société des sciences naturelles de Neuchâtel 96*, 135–147.

Preusser, F. & Kasper, H. U. 2001: Comparison of dose rate determination using high-resolution gamma spectrometry and inductively coupled plasma-mass spectrometry. *Ancient TL 19*, 17–21.

Pye, K. 1987: *Aeolian Dust and Dust Deposits*. 334 pp. Academic Press, London.

Rasmussen, S. O., Vinther, B. M., Clausen, H. B. & Andersen, K. K. 2007: Early Holocene climate oscillations recorded in three Greenland ice cores. *Quaternary Science Reviews 26*, 1907–1914.

Rietveld, H. M. 1969: A profile refinement method for nuclear and magnetic structures. *Journal of Applied Crystallography 2*, 65–71.

Rivière, A. 1977: *Méthodes Granulométriques, Techniques et Interprétation*. 170 pp. Masson, Paris.

Rolland, Y., Petit, C., Saillard, M., Braucher, R., Bourlès, D., Darnault, R. & Cassol, D. 2017: Inner gorges incision history: a proxy for deglaciation? Insights from Cosmic Ray Exposure dating (^{10}Be and ^{36}Cl) of river-polished surfaces (Tinée River, SW Alps, France). *Earth and Planetary Science Letters 457*, 271–281.

Rousseau, D. D., Derbyshire, E., Antoine, P. & Hatté, C. 2006: European loess records. In Elias, S. (ed): *Encyclopedia of Quaternary*, 1440–1456. Elsevier, Amsterdam.

Sanders, D. & Ostermann, M. 2011: Post-last glacial alluvial fan and talus slope associations (Northern Calcareous Alps, Austria): a proxy for Late Pleistocene to Holocene climate change. *Geomorphology 131*, 85–97.

Sanderson, D. C. W. & Murphy, S. 2010: Using simple portable OSL measurements and laboratory characterisation to help understand complex and heterogeneous sediment sequences for luminescence dating. *Quaternary Geochronology 5*, 299–305.

Schimmelpfennig, I., Schaefer, J. M., Akçar, N., Ivy-Ochs, S., Finkel, R. C. & Schlüchter, C. 2012: Holocene glacier culminations in the Western Alps and their hemispheric relevance. *Geology 40*, 891–894.

Schimmelpfennig, I., Schaefer, J. M., Akçar, N., Koffman, T., Ivy-Ochs, S., Schwartz, R., Finkel, R. C., Zimmerman, S. & Schlüchter, C. 2014: A chronology of Holocene and Little Ice Age glacier culminations of the Steingletscher, Central Alps, Switzerland, based on high-sensitivity beryllium-10 moraine dating. *Earth and Planetary Science Letters 393*, 220–230.

Schmidt, R., Weckström, K., Lauterbach, S., Tessadri, R. & Huber, K. 2012: North Atlantic climate impact on early Lateglacial climate oscillations in the south-eastern Alps inferred from a multi-proxy lake sediment record. *Journal of Quaternary Science 27*, 40–50.

Schwander, J., Eicher, U. & Ammann, B. 2000: Oxygen isotopes of lake marl at Gerzensee and Leysin (Switzerland), covering the Younger Dryas and two minor oscillations, and their correlation to the GRIP ice core. *Palaeogeography, Palaeoclimatology, Palaeoecology 159*, 203–214.

Smalley, I. J. 1995: Making the material: The formation of silt sized primary mineral particles for loess deposits. *Quaternary Science Reviews 14*, 645–651.

Spaltenstein, H. 1984: *Pédogenèse sur calcaire dur dans les Hautes Alpes calcaires.* Ph.D. thesis (N°540), Ecole polytechnique fédérale de Lausanne, 540 pp.

Spaltenstein, H. 1985: Caractérisation de deux sols alpins minces sur calcaire dur dans le lapiaz du Sanetsch. *Bulletin de la Société vaudoise des sciences naturelles 77*, 245–254.

Steinemann, O., Ivy-Ochs, S., Grazioli, S., Luetscher, M., Fischer, U. H., Vockenhuber, C. & Synal, H. 2020: Quantifying glacial erosion on a limestone bed and the relevance for landscape development in the Alps. *Earth Surface Processes and Landforms 45*, 1401–1417.

Toby, B. H. 2006: R factors in Rietveld analysis: how good is good enough? *Powder Diffraction 21*, 67–70.

Újvári, G., Stevens, T., Svensson, A., Klötzli, U. S., Manning, C., Németh, T., Kovács, J., Sweeney, M. R., Gocke, M., Wiesenberg, G. L. B., Markovic, S. B. & Zech, M. 2015: Two possible source regions for central Greenland last glacial dust. *Geophysical Research Letters 42*, 10399–10408.

Uppala, S. M. and 46 others 2005: The ERA-40 re-analysis. *Quarterly Journal of the Royal Meteorological Society 131*, 2961–3012.

Valla, P. G., Van Der Beek, P. A. & Lague, D. 2010: Fluvial incision into bedrock: Insights from morphometric analysis and numerical modeling of gorges incising glacial hanging valleys (Western Alps, France). *Journal of Geophysical Research: Earth Surface 115*, F02010, https://doi.org/10.1029/2008jf001210.

Vandenberghe, J. 2013: Cryoturbation structures. *In* Elias, S. A. (ed.): *The Encyclopedia of Quaternary Science 3*, 430–435. Elsevier, Amsterdam.

Wallinga, J., Bos, A. J. J., Dorenbos, P., Murray, A. S. & Schokker, J. 2007: A test case for anomalous fading correction in IRSL dating. *Quaternary Geochronology 2*, 216–221.

Wintle, A. G. & Murray, A. S. 2006: A review of quartz optically stimulated luminescence characteristics and their relevance in single-aliquot regeneration dating protocols. *Radiation Measurements 41*, 369–391.

Wirsig, C., Zasadni, J., Christl, M., Akçar, N. & Ivy-Ochs, S. 2016a: Dating the onset of LGM ice surface lowering in the High Alps. *Quaternary Science Reviews 143*, 37–50.

Wirsig, C., Zasadni, J., Ivy-Ochs, S., Christl, M., Kober, F. & Schlüchter, C. 2016b: A deglaciation model of the Oberhasli, Switzerland. *Journal of Quaternary Science 31*, 46–59.

Zerathe, S., Lebourg, T., Braucher, R. & Bourlès, D. 2014: Mid-Holocene cluster of large-scale landslides revealed in the Southwestern Alps by ^{36}Cl dating. Insight on an Alpine-scale landslide activity. *Quaternary Science Reviews 90*, 106–127.

Supporting Information

Additional Supporting Information may be found in the online version of this article at http://www.boreas.dk.

Table S1. Samples locations, corresponding geomorphic units and conducted analyses.

Table S2. Luminescence protocols.

Table S3. Stratigraphical description and field interpretation of the sedimentological units forming the ARP high-elevation platform deposit.

Table S4. Stratigraphical description and field interpretation of the sedimentological units forming the upper 4.5 m of the CRE alluvial fan.

Table S5. Luminescence signal intensities measured for the CRE and ARP sites using the SUERC portable OSL reader (Sanderson & Murphy 2010), and following the measurement sequence of Muñoz-Salinas *et al.* (2014).

Table S6. Grain-size distributions of CRE (G1–G6; S6A) and ARP (G7 and G8; S6B) samples.

Table S7. XRD bulk mineralogical compositions of CRE (CRE01–CRE16), ARP (ARP01 and ARP03) and bedrock (L1–L2: siliceous limestone, S1–S2: calcareous shale) samples.